Masters' Thesis

Changes in Synaptic Connectivity during Ultradian Growth Hormone Secretion are Correlated with Changes in Astrocytic Coverage of Neurons as Seen in Super-Resolution and Electron Microscopy

Klaudia Bednarz
Department of Anatomy and Cell Biology
Research conducted at the Montreal Neurological Institute
McGill University, Montreal
July 2019

A thesis submitted to McGill University in partial fulfillment of the requirements of the
degree of Master of Science in Cell Biology

Supervised by Thomas Stroh, Ph.D.

Acknowledgements

This project would not have been possible without the continuous support of my supervisor, Dr. Thomas Stroh. His microscopy knowledge, trust, confidence, ability to gather people and resources made the ideas bloom and move forward.

I would also like to thank my friend and PhD student, Walaa Alshafie, for her everyday support, encouragement and scientific input.

Thanks to the talented undergraduate colleague, Sean Goldfarb, and a Masters' intern, Théotime Desserteaux, for working hard with me on the project. You have a bright future and I cannot wait to see your next scientific endeavors.

To Carl Ebeling, staff at Bruker and Sarah Aufmkolk, a post-doctoral researcher at the Montreal Neurological Institute. Thank you for your patience, willingness to help, and continuous scientific support in single molecule localization and dSTORM microscopy.

To my advisory committee, Dr. Maia Kokoeva, Dr. Khanh Huy Bui and my mentor, Dr. Nathalie Lamarche-Vane. Thank you for your support and genuine interest in my project.

Thanks to our collaborators, Dr. Florian Storch and his PhD student Pratap Singh Markam, for providing us with animals and allowing us to perform all animal experiments and ELISA measurements in their lab. Special thanks to Pratap for spending the time to show me blood collection in animals and ELISA measurements.

I thank the lab of Dr. Michael Petrides and especially Jennifer Novek, for helping train us and sharing their lab equipment.

To Jeannie Mui, Weawkamol Leelapornpisit and Kelly Sears for aiding in electron microscopy sample preparation and focus ion-beam imaging.

I would also like to thank Naomi Takeda, our administrative assistant, for her everyday support with lab orders and assistance with regards to the completion of my degree.

Finally, thanks to Dr. John Presley for evaluating my initial thesis.

Contribution of Authors

I performed all animal habituation, blood collections, ELISA hormone measurements, dSTORM staining, imaging, analysis, and electron microscopy imaging.

I, with the help of Walaa Alshafie, designed all experiments, set parameters for analysis and interpreted results. Moreover, Walaa Alshafie performed statistical analysis and created graphs on pages 55-57.

Dr. Thomas Stroh and Walaa Alshafie assisted in mouse perfusions and brain extraction.

Sean Goldfarb and Théotime Desserteaux analyzed the electron microscopy and focused ion-beam data. Théotime Desserteaux also programmed plug-ins for the “R” statistical software for dSTORM data analysis and corrected the French version of the abstract.

Jeannie Mui performed electron microscopy sample preparation and wrote methods for this part of the thesis.

Weawkamol Leelapornpisit performed focused-ion beam imaging and wrote methods for this part of the thesis.

I wrote the thesis and Dr. Thomas Stroh reviewed the initial version.

Table of Contents

1. Introduction

4. Results

Abstract

The secretion of growth hormone (GH) occurs in a pulsatile manner throughout the day in mammals. Multiple mechanisms must come together to ensure repeated pulses and thus hormonal homeostasis. The hypothalamus serves as a “control center” for this pulsatility via the synthesis and secretion of GH-releasing hormone (GHRH) and somatostatin (SS) that act reciprocally to influence GH secretion from the pituitary gland into the bloodstream. Moreover, it is well known that synaptic transmission in the hypothalamus undergoes cyclical changes in parallel with the circadian and ultradian rhythms of hypothalamic hormone secretion. Our lab and others have shown in the past that changes in the number and density of synaptic contacts on hypothalamic neurons may be the source of these rhythmic changes in synaptic transmission. However, except for a few examples such as synaptic plasticity in magnocellular oxytocin neurons during lactation, the exact cellular mechanism of this plasticity is little defined. Also, the molecular architecture of synapses in this area as well as its potential rhythmic changes are largely unknown. Interestingly, glial cells have been recently implicated not only as the supporting cells of the brain but also having a functional role in the development, maintenance, and plasticity of synapses.

As such, with the advent of readily available techniques of super-resolution microscopy, easily allowing the simultaneous imaging of multiple synaptic markers in a large field of view containing many synapses, we imaged and analyzed brain tissue of animals timed for GH secretion using direct Stochastic Optical Reconstruction Microscopy (dSTORM). To evaluate tissue context for a potential role of glial cells, we performed electron microscopy (EM) and Focused Ion-Beam Scanning Electron

Microscopy (FIB-SEM). We hypothesized that more inhibitory synapses will be seen during trough (low levels) of GH secretion and more excitatory synapses during peak (high levels) of GH secretion. We also hypothesized that more astrocytic processes will be seen between neuronal membranes when hormone levels are low. We collected brain tissue from 18 animals with prior measurements of blood GH levels using sensitive tail-clip ELISA analysis. dSTORM imaging and analysis of Gephyrin and VGAT (inhibitory synapse) and VGLUT2 and PSD-95 (excitatory synapse) was performed. EM of tissue from three mice was performed. FIB-SEM collection of 700-1000 frames from two mice was completed.

With dSTORM imaging and analysis, we observed synaptic and non-synaptic cluster populations of Gephyrin, VGAT, VGLUT2 and PSD-95. The surface area of most clusters was in the range of 0.01 to 0.15 um^2. Non-synaptic cluster populations were below 0.01 um^2. During troughs of GH secretion, 66% of all synapses were inhibitory and 34% excitatory. During peaks, 71% of all synapses were excitatory and 29% inhibitory. Moreover, there was an increase of 40% in the association of non-synaptic clusters to form a “functional” excitatory synapse cluster during high levels of GH secretion, which indicates a potential mobilization of non-synaptic cluster populations during peak of GH secretion. Lastly, with the use of EM, on average 4.4 astrocytic processes were found during low levels of GH and 1.8 astrocytic processes during high levels of GH between neuronal membranes.

Résumé

La sécrétion de l'hormone de croissance (GH) se produit de manière pulsatile tout au long de la journée chez les mammifères. De multiples mécanismes doivent être réunis pour garantir des pulses répétés et donc l'homéostasie hormonale. L'hypothalamus sert de «centre de contrôle» de cette pulsatilité via la synthèse et la sécrétion de «Growth Hormone-Releasing Hormone» (GHRH) et de somatostatine (SS), qui agissent réciproquement pour influencer la sécrétion de GH de la glande pituitaire dans le sang. De plus, il est bien connu que la transmission synaptique dans l'hypothalamus subit des changements cycliques parallèlement aux rythmes circadien et ultradien de la sécrétion d'hormone hypothalamique. Notre laboratoire et d'autres ont montré dans le passé que des changements dans le nombre et la densité des contacts synaptiques sur les neurones hypothalamiques pourraient être à l'origine de ces changements rythmiques dans la transmission synaptique. Cependant, à l'exception de quelques exemples tels que la plasticité synaptique dans les neurones d'ocytocinemagnocellulaires pendant la lactation, le mécanisme cellulaire exact de cette plasticité est peu défini. Cela dit, l'architecture moléculaire des synapses dans ce domaine ainsi que ses potentiels changements rythmiques sont en grande partie inconnus. Il est intéressant de noter que les cellules gliales ont récemment été considérées non seulement en tant que cellules de soutien du cerveau, mais également comme ayant un rôle fonctionnel dans le développement, le maintien et la plasticité des synapses.

Ainsi, avec l'apparition de techniques de microscopie à super-résolution de plus en plus accessibles, permettant assez facilement l'imagerie simultanée de multiples

marqueurs synaptiques dans un grand champ de vision contenant un grand nombre de synapses, nous avons visualisé et analysé le tissu cérébral des animaux dont la concentration plasmatique en GH a été mesurée avec “direct Stochastic Optical Reconstruction Microscopy” (dSTORM). Pour évaluer le rôle potentiel des cellules gliales dans le contexte tissulaire, nous avons effectué de la microscopie électronique (EM) et de la microscopie électronique à balayage par faisceau ionique focalisé (FIB-SEM). Nous avons émis l’hypothèse que davantage de synapses inhibitrices seraient observées lors du nadir (faible concentration) de GH plasmatique et plus de synapses excitatrices lors du zénith (concentration élevée) de GH plasmatique. Nous avons également émis l’hypothèse que davantage de cellules gliales seraient observées lorsque les niveaux d’hormones seraient bas. Nous avons recueilli le tissu cérébral de 18 animaux avec des mesures préalables des taux de GH sanguins en utilisant une analyse ELISA par pince de queue. L'imagerie dSTORM et l'analyse de Gephyrin et VGAT (synapse inhibitrice) et de VGLUT2 et PSD95 (synapse excitatrice) ont été réalisées. La ME d'un tissu de trois souris a été réalisée. La collection FIB-SEM de 700 et 1000 images correspondant à deux souris a été complétée.

Avec l’imagerie et l’analyse dSTORM, nous avons observé des populations d’agglomérations (cluster) synaptiques et non synaptiques de Gephyrin, VGAT, VGLUT2 et PSD95. La surface spécifique de la plupart desclusters était comprise entre 0,01 et 0,15 µm^2. Les populations de clusters non synaptiques étaient inférieures à 0,01 µm^2. Au cours du nadir de GH, 66% de toutes les synapses étaient inhibitrices et 34% excitatrices. Au zénith, 71% des synapses sont excitatrices et 29% inhibitrices. De plus, l'association de clusters non synaptiques a augmenté de 40% pour former des «synapses fonctionnelles» lors de fortes sécrétions de GH, ce qui indique une mobilisation potentielle de populations de clusters non synaptiques pendant le pic de sécrétion de GH. Enfin, avec l'utilisation de l'EM, en moyenne 4.4 processus astrocytaires ont été trouvés (par image, avec un grossissement de 4800x) au nadir de GH et 1.8 processus astrocytaires lors du zénith de GH.

1. INTRODUCTION

1.1 Growth Hormone

Growth Hormone (GH), as its name suggests, is a hormone involved in the fundamental physiological process of growth, metabolism and development (1). It is not surprising that deficiency of GH can lead to serious growth retardation, diminished cognitive functions, delayed development (2) and its excess to conditions such as gigantism and acromegaly (3).

GH polypeptide consists of 191 amino acids and is known to act in both humans and animals. It is secreted within the lateral wings of the anterior pituitary by somatotropic cells and transported by blood to various targets, such as bone, liver, adipocytes and muscles (1). Its effects on target tissue are either direct – where GH binds to its receptor and elicits intracellular signaling – or indirect – primarily mediated by Insulin Like Growth Factor-I (IGF-1) secreted from the liver and other tissues in response to GH. Both signals eventually lead to tissue growth via numerous pathways, such as increased uptake of amino acids from blood, breakdown of stored fat and glycogen, bone growth by chondrocyte stimulation, etc. (1).

The regulation of GH release starts at the level of the hypothalamus, where Growth-Hormone-Releasing-Hormone (GHRH) is synthesized to stimulate and Somatostatin (SS) to inhibit the secretion of GH. The feedback of GH on GHRH and SS is aided by central and peripheral regulators to meet the body’s physiological GH demands (4). Neurons that release GHRH reside in the arcuate nucleus of the hypothalamus with dense terminal projections in the median eminence (5), a site of

GHRH release into the hypophyseal portal venous blood surrounding the anterior pituitary gland. SS neurons are mainly found in the arcuate nucleus and the periventricular nucleus of the hypothalamus.

The intimate interplay between GHRH and SS determines the pattern of GH secretion (6). In fact, GH secretion occurs in a pulsatile manner, with peaks (high levels of GH) and troughs (low levels of GH) of secretion in every species examined until now (7). This pulsatility occurs in an ultradian manner and its timing and duration are sex- and species-specific, with peaks every 3.3 hours in male rats (7) and every 2.5 hours in male mice (2). In humans, men exhibit a large nocturnal secretion of GH followed by small pulses every 2 hours (8), whereas women demonstrate regular pulses throughout the 24-hour period (9). Interestingly, GHRH neurons are not inherently rhythmic at the electrical level, since no electrical oscillations were detected in patch-clamp studies *in situ* (10, 11). Therefore, it is believed that GH pulses result in part from the periodic, central inhibition of GHRH by SS via somatostatin receptor subtype 1 and 2 (sst1 and sst2) (12,13). GHRH neurons also receive abundant synaptic inputs from neurotransmitter-releasing neurons (GABA and glutamate) (10). Moreover, GH secretion is inhibited by glucocorticoids in humans and animals, however, *in vitro* glucocorticoids increase the levels of GH (14). These opposite actions are mediated at different sites, with modulation of hypothalamic SS involved in inhibition and direct actions on the pituitary involved in stimulation. *In vivo*, the predominant action is through the inhibitory influences on SS (15).

Our lab has shown in the past that in parallel with the ultradian pattern of GH secretion, synaptic connectivity of the arcuate nucleus of male rats also exhibit ultradian dynamics (16). As such, proportions of symmetric (inhibitory) and asymmetric (excitatory) synaptic profiles that contact GHRH-positive neurons in the arcuate nucleus are different during peaks and troughs of GH secretion: 50% symmetric and 50% asymmetric synapses are seen during peaks and 70% symmetric and 30% asymmetric synapses during troughs of GH secretion. However, the mechanism and significance of these changes have not been yet explored.

Moreover, an interesting observation has been made in another system of pulsatile hormone secretion: the oxytonergic (OT) system in lactating versus non-lactating animals (17). There, under a basal condition of neurosecretion (troughs), fine lamella-like processes of astrocytes separate neuronal membranes in the supraoptic nucleus (SON) of the hypothalamus. In contrast, during intense hormone secretion (peaks), neuronal membranes are directly juxtaposed and not separated by astrocytes in the SON (17). Thus, due to the increased membrane contacts between neurons during peaks, more synapses can form and potentially drive excitation and hormone secretion. Whether the membrane juxtaposition is simply a result of glial retraction remains unanswered. However, it is unlikely that this is a result of neuronal hypertrophy during intense hormone secretion (where astrocytes would be passively squeezed out), because somata of both - oxytocinergic and vasopressinergic neurons hypertrophy when stimulated, yet an increased incidence of juxtapositions is observed only for the former (17).

1.2 Glial cells, astrocytes and the tripartite synapse

Glial cells are non-neuronal cells in the central and peripheral nervous system and were discovered in 1856 by Rudolf Virchow in his quest to find the “connective tissue of the brain” (18). In the central nervous system, glial cells include oligodendrocytes, astrocytes, ependymal cells and microglia; in the peripheral nervous system, these include Schwann cells and satellite cells (19). Glial cells were traditionally considered the “glue” of the nervous system. Indeed, they surround and isolate neurons and hold them in place, supply nutrients and oxygen to neurons and clear debris from the extracellular space (20).

However, over the past 20 years, there has been a growing consensus and appreciation for the role of glial cells in synaptic transmission (21). In the peripheral nervous system, synapses are surrounded by non-myelinating Schwann cells, and in the central nervous system (CNS) by astrocytes. The association of astrocytes with synapses in the CNS is referred to as the “tripartite synapse”. As such, astrocytes are thought to be active participants in synaptic transmission.

Indeed, perisynaptic processes of astrocytes express active G-protein-coupled receptors that can sense and respond to neurotransmitters released into the synaptic cleft during synaptic activity and release gliotransmitters that in turn interact with synaptic elements (22). Moreover, astrocytes control synapse formation and specificity, and several studies unraveled various factors secreted by astrocytes that participate in this process. One of those factors, called thrombospondin (TSP), induces the formation of structurally normal but postsynaptically silent synapses (23). In culture, TSPs were found to increase synapse numbers and removal of TSPs from medium that is astrocyte-conditioned diminished synaptogenic activity of the system (23). However, it is known that astrocytes can induce both, pre- and post-synaptic activity (not only post-synaptically silent synapses), therefore it is believed that another signal secreted by astrocytes allows for the conversion of post-synaptically silent synapses to active ones, most likely by the insertion of glutamate receptors at postsynaptic sites. However, the identity of this signal is unknown (24). Astrocytes are also able to regulate synapse formation through a mechanism in which a neuron can only respond to a synaptogenic signal once a physical contact with an astrocyte is established (25). Although the exact mechanism of this is not yet well understood, a study of neurons dissociated from the embryonic hippocampus revealed that it is the activation of protein kinase-C signaling through integrin-binding of astrocytes and neurons that facilitates excitatory synapse formation (26). Astrocytes also play an important part in establishing synaptic connectivity in disease states. For example, after ischemic brain injury, reactive astrocytes revert to an immature state and start to express TSP molecules (TSP1 and TSP2) that facilitate synapse formation. This upregulation of TSP was shown to be the result of purinoceptor signaling and mechanical stimulation in cultured astrocytes (27). These proteins could be also upregulated via a similar mechanism *in vivo* upon injury.

Recently, it was shown that astrocytes in the hypothalamus play an important role in the regulation of body energy homeostasis (28). The hypothalamus is a major site of signal integration from the environment (ex. temperature, light, glucose and nutrients in general) with hormonal and neural signals from inside the body (29). For example, astrocytes found within the hypothalamus actively cooperate with specialized neurons that are glucose-sensitive in detecting the circulating levels of glucose (30). The crucial role of astrocytes in this process was shown by lowering the expression of GLUT1 and GLUT2 in rodents, where systemic hyperglycemia was observed. This effect was reversed with a virus-mediated reintroduction of GLUT1 into hypothalamic astrocytes (31). Further evidence supporting the claim that astrocytes are required for effective glucose sensing comes from connexin knock-out studies (32). Connexins are proteins that form channels to allow for the transmission of signaling molecules and nutrients over long distances between astrocytes (32). When connexin 43 was ablated with a specific siRNA probe in the arcuate nucleus of the hypothalamus, the release of insulin from the pancreas in response to central glucose upregulation was diminished (33). As such, one might conclude that astrocytic presence and intercommunication within the hypothalamus is required for proper central glucose sensing.

Importantly, astrocytes express receptors for hormones involved in energy homeostasis and this suggests that they might be involved in hormonal regulation of body homeostasis. These receptors include leptin (34), thyroid hormone (35), insulin-like growth factor-1 (36), insulin (37) and glucagon-like peptide-1 (38). However, it is not yet fully understood how the activation of these receptors impacts metabolism. Nevertheless, a few studies have shown that there are distinct morphological changes in hypothalamic astrocytes following hormonal stimulation. For example, the extent to which astrocytes enwrap adjacent neurons following changes in circulating levels of leptin shifts dramatically and thus alters the neuronal electrophysiological response. This was shown by chronic intra-cerebroventricular leptin administration in male rats for two weeks. An increase in astrocyte structural proteins, GFAP and vimentin was induced. This was inversely related to modifications in synaptic protein densities (39).

Moreover, in anorexigenic POMC-expressing cells of the arcuate nucleus regulating feeding behavior, a greater number of inhibitory synaptic inputs were found in the POMC neurons of lean rats that were vulnerable to diet-induced obesity compared to lean rats that were resistant to diet-induced obesity (40). Moreover, when exposed to a high-fat diet, these POMC cells of the same rats lost synapses, while more connections were seen in rats resistant to diet-induced obesity. In rats vulnerable to diet-induced obesity, the loss of synapses on POMC neurons triggered by high-fat diet was also associated with increased glial ensheathment of POMC neurons. As such, a high-fat diet had a major impact on the morphology of the arcuate nucleus in vulnerable animals (40). Lastly, as discussed earlier and relevant in the discussion of homeostatic control by astrocytes, in magnocellular oxytocin neurons, astrocyte processes are seen during low hormone levels and fewer processes are seen during hormone stimulation (lactation). As such, with a decreased number of astrocytes, more synapses can form and drive excitation (17).

1.3 Super-resolution microscopy

“Seeing is believing” and advances in cell biology would not be possible without advances in microscopy. In fact, some of the recent evolution in microscopy has lead to the discovery of several novel cellular structures, including a periodic actin-spectrin membrane skeleton in neurons (41), distinct chromatin folding for different epigenetic states (42) or protein aggregation studies in Alzheimer’s disease (43). The perception of what is possible in terms of spatial resolution in the optical microscope has dramatically changed over the past few decades. When Carl Zeiss and Otto Schott developed their first apochromat lens microscope in 1886, they were convinced that resolution below 200nm was unachievable due to Ernst Abbe's theory of diffracted-limited resolution (which has been accepted until today) (44). However, new methods to bypass the diffraction limit were later developed. One of them was lead by Ernst Stelzer and the Zeiss company, who built their first confocal microscope in 1985 by developing a pinhole that filtered out-of-focus light (45).

Fifteen years after the confocal microscopy revolution, the first super-resolution technique was developed. In general, super-resolution techniques break the diffraction limit by either spatially or temporally modulating the excitation or activation light (46). A real breakthrough that resulted in the Nobel Prize in Chemistry, came from the lab of Stefan Hell in 2000. He introduced a high-energy method known as Stimulated Emission Depletion (STED) that breaks the diffraction limit by the spatial modulation of light (46). In STED, a narrow beam of light excites a small portion of the sample, while simultaneously another "doughnut-shaped" high-energy beam of longer wavelengths is applied around the first beam. This doughnut-shaped beam comes from a second laser called "the STED laser". This laser pushes light-excited fluorophores back to the ground state only at the perimeter of the point spread function (PSF) of a fluorophore (the center of the PSF continues emitting fluorescence) (46). This optically modifies the PSF to reduce its effective diameter, thus removing any out-of-focus light. One of the first studies published using STED achieved a resolution of 100nm in the lateral direction while imaging nanocrystals (47). The best resolution using STED achieved so far in a biological context is 20 nm (48).

Six years later, in 2006, a co-recipient of the Nobel Prize in Chemistry Eric Betzig developed another super-resolution method – called the photoactivatable localization microscopy (PALM) (49) and Zhuang Xiang developed an alternative approach called Stochastic Optical Reconstruction Microscopy (STORM) (50). Both methods rely on what is called “single molecule localization” (SML), where only a sparse subset of molecules is activated at a given time. This activation is repeated over thousands of frames (where a different subset of molecules is activated each time) and frames are then merged to form the final image. The difference between PALM and STORM is that the former uses genetically encoded photoswitchable fluorophores (such as GFP) and the latter utilizes antibodies dye pairs (activator and a reporter) that can be switched “on” and “off”. Indeed, antibody selection is a key process in successful STORM imaging, since the photochemical properties of the fluorophore must be exploited to induce a non-emissive “dark” state (50). The most common activator-reporter dye pair is Cy3-Cy5, where a strong red laser switches Cy5 to its dark state and a green laser then converts Cy5 back to its fluorescent state, given that Cy5 is near Cy3. Upon reactivation with the green laser, Cy5 is imaged with a red laser before being switched off again, and the cycle repeats (51). Cy3-Cy5 dye pairs can be imaged for many cycles without photobleaching.

Of great importance to our study, an alternative approach to STORM called dSTORM (direct STORM) allows excitation of conventional organic fluorophores directly, without the need of the conjugated activator-reporter pair. In this scenario, the “dark” state is achieved as the final step of a molecule’s electronic transition upon light excitation. As such, when excited by light, electrons are moved to higher-energy orbits and can return to the initial orbit by emitting fluorescence or they can transition back through what is called a “triplet state” without fluorescence. It is from the triplet state that many fluorophores can be reduced to a dark and stable state suited for dSTORM imaging. To aid in the chemical reduction of fluorophores to the dark state, a special buffer consisting of reducing agents and oxygen scavengers must be added during imaging (what we call a “blinking buffer”). The excitation laser of appropriate wavelength “pushes” fluorophores into the dark state and a 405-activation laser facilitates their return to the fluorescent state (52), allowing to capture thousands of frames that are then reconstructed into a single image. The best suited organic fluorophores currently on the market for dSTORM imaging are Alexa 647 and CF 568. They yield the best results because they can survive many photo-switching cycles before bleaching, have a high photon count (i.e. are bright) and low duty cycle (stay “on” for a short time once activated) (53).

The expansion of dSTORM to 3-D imaging was another important step in the evolution of this technique. Many strategies have evolved for 3D STORM, including imaging in two or more different focal planes (for example, the biplane imaging strategy on the Vutara microscope at our institute), interferometry, tilted mirrors and convolution of the point-spread function with a more complex mathematical model (54). In biplane imaging, the lateral resolution of the image is independent of the axial position. This is because by imaging two focal planes of fluorophores (one over-focused and one under-focused), a three-dimensional PSF can be fitted (54). The imaging depth that can be achieved in this technique is about 800 nanometers in the z-direction without scanning and with the addition of axial scanning techniques, several micrometers (54).

As such, relevant to our study, dSTORM allows for high-precision imaging of synapses in a large field of view. Considering the size of the synaptic cleft of ~20-40nm from electron microscopy studies (55) and the thickness of the post-synaptic density (PSD) of ~25-50 nm, it is clear why this technique is ideal for imaging synapses. Moreover, unlike in the electron microscope where the field of view is limited, in the dSTORM setup at our institute, a 100x oil lens provides a field of view of 20 μm x 20 μm and a 3D thickness of 1 μm. Therefore, larger numbers of synapses can be recorded in one frame.

In addition to STED, PALM and STORM, other super-resolution techniques are now commonly used. One of them is Structured Illumination Microscopy (SIM). SIM works by using a stripe-patterned illumination to excite the sample and the pattern's position is rotated several times to record a fluorescent signal at each position. Because of light interference between the patterned illumination and the sample, "Moiré" patterns are produced. These patterns contain high frequency spatial information that would otherwise be non-decipherable through diffraction-limited imaging and produce a lateral resolution of 100-130 nm. In 3-D, the patterned light is rotated in three dimensions and the axial resolution that can be achieved is in the range of 250-350 nm (56).

1.4 Electron Microscopy and Focused-Ion Beam

Although super-resolution microscopy allows visualization of structures at an astounding resolution of 20 nm, it does not permit visualization of tissue context and morphology, since only a few selected structures can be visualized at one time with fluorescent protein labeling or expression. As such, scientists often resort to the power of electron microscopy. With a simple contrast enhancement, one can see the entirety of the tissue of interest at a theoretical resolution of 1 Angstrom. Electron microscopes use a beam of accelerated electrons as a source of illumination. Since the wavelength of electrons is about 100,000 times shorter than that of light, the resolving power of an electron microscope is much greater than any of the super-resolution techniques (57). However, a downside to this is the narrow field of view. Once accelerated, electrons are focused using a magnetic field. In a Scanning Electron Microscope (SEM), unlike a Transmission Electron Microscope (TEM), the sample is then scanned by the electron beam across a rectangular area of the specimen (what is called a raster scan) (58). The information about the specimen comes from the various sources of scattered electrons or energy loss once the beam hits the sample; including, but not restricted to, secondary electrons, backscattered electrons and heat (58).

Electrons are not the only particles that can be accelerated and focused using a magnetic field (59). An ion with a net positive or negative charge can also “do the job”. This is the principle behind the Focused Ion Beam (FIB). In this approach, a beam of ions is focused on the sample. Due to the extremely high energy, the focused ion beam directly “mills” or removes layers of the specimen surface via the sputtering process. This milling can be controlled with extreme precision by controlling the energy and intensity of the ion beam (60). FIB becomes very powerful when combined with SEM in a dual-beam system. Here, electron and ion beams intersect at an angle at a point near the surface of the sample, allowing for immediate high-resolution imaging of the new surface that is unraveled with each FIB beam. This means that by acquiring hundreds of images with tissue being removed after each individual image, one can obtain a 3D view that is not limited by the axial resolution of the microscope (60).

2. RATIONALE AND HYPOTHESIS

In view of the above, we postulated whether a mechanism responsible for changes in synaptic connectivity that occur in parallel with ultradian changes in GH secretion involves astrocytes. We stipulated whether astrocytic retraction during peak of GH secretion allows for more excitatory synapses to form, thus changing the absolute numbers of excitatory synapses (and thus the relative number of excitatory to inhibitory synapses) and participating in the regulation of GH periodic release. We hypothesized that during high levels of GH (peaks), we will see more excitatory synapses contacting GHRH neurons and equal or higher numbers of inhibitory synapses during low levels of GH (troughs). We also hypothesized that there will be more astrocytic processes intertwined between neuronal membranes, dendrites or axons during troughs of GH secretion and fewer during peaks. This astrocytic retraction during peaks of GH would enable more excitatory synapses to form and potentially drive excitation.

3. MATERIALS AND METHODS

Blood and tissue collection

All animal procedures were approved by the Animal Care Committee of McGill University and conducted in compliance with the guidelines of the Canadian Council of Animal Care. Adult (8 to 10-week-old) C57BL/6 mice (Charles River Canada, Saint Constant, QC) were group-housed (n = 4) for at least two weeks before the experiment under a 12h light, 12h dark cycle (lights on at 08:00 A.M and off at 08:00 P.M). Room temperature was maintained at 20 ± 2°C. Mouse chow and tap water were available *ad libitum*. To minimize stress, prior to all experiments, mice were habituated to the test environment (tail massage, human touch and smell) for 10 days, 15 minutes each day. Habituation was done by the same person who performed all subsequent experiments.

To determine plasma growth hormone levels, tail-clip whole blood sample collection and ELISA analysis were used, as described previously (61). As such, the tip of a mouse's tail (~2 mm) was cut off with a surgical blade and 2 µl of blood was drawn with a pipette. The blood was immediately transferred to an eppendorf containing 58 µl of 0.05% PBS-Tween 20 and placed on dry ice until the end of the collection period. The samples were then placed at –80°C until GH levels were analyzed by ELISA. The tail was cut once and subsequent blood withdrawals were done from the same wound every 15 or 20 minutes, by gently squeezing the tip of the tail. When the blood flow was obstructed by the formation of a clot towards the end of the collection period, the wound was gently opened with gauze soaked in saline. Blood was collected for at least 2 hours and up to 6 hours and 20 minutes before sacrificing the mouse. The time of sacrifice was chosen randomly, based on the results of our preliminary experiments that characterized the profile of GH in mice over a 6-hour period (see Results – Plasma GH Levels). Immediately after the last blood sample collection, the mouse was anesthetized with an intraperitoneal injection of Ketamine/Xylazine/Acepromazine followed by a transaortic perfusion with 4% PFA in 0.1 M phosphate buffer for super-resolution microscopy or 2% PFA + 2% glutaraldehyde in 0.1 M phosphate buffer for electron microscopy. Brains were immediately extracted and post-fixed in the same fixative overnight at 4°C. The next day, brains were placed in 30% sucrose solution in 0.1 M phosphate buffer until the tissue had sunk (overnight), then snap-freezed at –40°C in isopentane and stored at –80°C until sectioning. 30 µm sections were obtained with Leica Ultramicrotome for super-resolution microscopy and 200 µm vibratome sections were obtained for subsequent electron microscopy embedding and sectioning procedures.

Growth Hormone ELISA measurement

Plasma GH concentrations were measured using a sensitive sandwich ELISA assay as described earlier (61). As such, a 96-well plate (Corning Inc., 9018) was coated overnight at 4°C with 50 µl monkey anti-rat GH antibody (AFP411S, NIDDK-NHPP, Torrance, CA) at a final dilution of 1: 40,000. Each well was subsequently incubated with 200 µl blocking buffer [5% skim milk powder in 0.05% PBS-Tween 20] for 2 hours at room temperature. A standard curve was generated using 2-fold serial dilutions of mouse GH (reference preparation, AFP-10783B, NIDDK-NHPP) in 0.05% PBS-Tween 20 supplemented with 1ng/ml normal goat serum (NGS) to a final concentration of 0.2% NGS-Tween 20. 50 μl of standard curve solutions in duplicates or blood samples in singlets were loaded to the plate and incubated for 2 hours at room temperature on an orbital shaker. After washing, bound standards and samples were incubated with 50 μl detection antibody (rabbit antiserum to rGH, AFP5672099, NIDDK-NHPP) at a final dilution of 1:40,000 in a blocking buffer for 90 minutes. The bound complex was incubated with 50 μl horseradish peroxidase-conjugated antibody (Goat anti- rabbit BioRad) at a final dilution of 1:2000 in blocking buffer for 90 minutes. Addition of 100 μl O-phenylenediamine (00-2003; Invitrogen, Carlsbad, CA) substrate to each well resulted in an enzymatic colorimetric reaction. This reaction was stopped by addition of 50 μl 3 M HCl, and the absorbance was read at dual wavelengths of 490 nm and 650 nm with a microplate reader. The concentration of GH in each well was calculated by regression of the standard curve.

Immunofluorescence staining for dSTORM imaging

30 μm mouse brain sections representing approximately Bregma –1.06 mm to –2.54 mm of the "Mouse Brain" G. Paxinos atlas (62) and containing the tuberal hypothalamus (63) with the arcuate nucleus were used for all experiments. Sections were identified visually, according to their position within the brain and the tissue morphology (shape of the third ventricle, position of lateral ventricles, distinct mound of the median eminence). Each section was first incubated with 0.1% $NaBH_4$ in 0.1M TBS, then washed three times in 0.1M TBS and incubated in blocking buffer containing 10% NGS, 3% BSA and 0.1% Triton X-100 in 0.1 M TBS for 2 hours. Sections were then incubated with primary antibody cocktail containing primary

antibodies, 0.1% Triton X-100 and 2% NGS in 0.1 M TBS at 4°C overnight. Each section was triple-stained with a pair of antibodies against a pre-and post-synaptic marker of either inhibitory or excitatory synapses plus an antibody against the Growth-Hormone-Releasing-Hormone (GHRH) to demarcate GHRH cells.

Primary antibodies used included monoclonal mouse anti-Gephyrin at a dilution of 1:500 (to stain pre-synaptic terminals of inhibitory synapses), monoclonal guinea pig anti-VGAT at 1:1000 (post-synaptic terminals of inhibitory synapses), polyclonal guinea pig anti-VGLUT2 at 1:500 (pre-synaptic terminals of excitatory synapses) (all purchased from Synaptic Systems, Göttingen, Germany), mouse monoclonal anti-PSD95 at 1:500 (post-synaptic terminal of excitatory synapses) (Abcam, Cambridge, United Kingdom) and polyclonal rabbit anti-GHRH at 1:500 (AB5343 AB Clonal, Woburn, USA).

The following day, sections were washed three times for 5 minutes in 0.1 M TBS + 0.1% Triton X-100, then incubated with secondary antibody solution containing secondary antibodies, 0.1% Triton X-100 and 2% NGS in 0.1M TBS for 1.5 hours. Secondary antibodies used included Alexa 647 goat anti-guinea pig IgG at 1:500 and CF 568 goat anti-mouse IgG at 1:500 and Alexa 488 goat anti-rabbit at 1:500 (all purchased from Life Technologies, Grand Island, New York). Next, sections were washed twice in a solution of 0.1M TBS and 0.1% Triton X-100 and then three more times with 0.1M TBS, followed by a 30-minute post-fixation in 4% PFA in 0.1M SPB. Finally, sections were washed three times for 10 min in 0.1M TBS and stored in scale U2 clearing buffer (64) for two to maximum seven days at 4°C before imaging.

Electron microscopy sample preparation

200 µm vibratome sections were fixed in 2.5% glutaraldehyde in 0.1 M sodium cacodylate buffer, washed with 0.1 M cacodylate washing buffer, then post-fixed with 1% osmium tetroxide for 1 hour. Sections were then washed with dH_2O and block-stained with 1% uranyl acetate for 1 hour. Dehydration with ethyl alcohol in series of increasing concentrations from 30% to 100% followed. Next, sections were infiltrated with 1:1, 3:1 (EPON:alcohol) and 100% EPON, then transferred to flat-embedding moulds and polymerized at 65°C for 48 hours. Finally, a Leica Microsystems Ultracut EM UCT ultramicrotome was used to prepare 90-nm thick *en face* sections and transferred onto slotted TEM grids with a Formvar support film.

dSTORM imaging

Sections were transferred from the clearing agent (scale U2 buffer) to 0.1 M TBS and mounted on a #1.5 circular coverglass, 25 mm in diameter (cat. #72225-01, Electron Microscopy Sciences). 1 mL of imaging buffer (what is also called a “blinking buffer”) was prepared prior to imaging and a big drop was added onto the section. Blinking buffer consisted of 20mM MEA in 50mM Tris-HCl (pH 8), 10mM NaCl, 1% (v/v) 2-mercaptoethanol (Sigma Aldrich) and 1X Gloxy solution, all diluted in a buffer containing 50mM Tris-HCl at pH8, 10mM NaCl and 10% (w/v) glucose. Gloxy solution was prepared as a 50X stock containing 8440 AU of glucose oxidase type seven from Aspergilius (Sigma Aldrich) and 70200 AU of catalase from bovine liver (Sigma Aldrich) in a buffer containing 50mM Tris-HCl (pH 8) + 10mM NaCl. A second #1.5 coverglass, 25 mm in diameter was added on top of the first one (to create a "sandwich" of coverglass-brain section-coverglass). This prevented the section from moving during imaging. As the "blinking buffer's" redox ability diminished after approximately 1 hour of imaging, fresh buffer had to be added every hour to the section.

dSTORM imaging was performed on a Vutara SRX-350 microscope equipped with a 60X water-immersion objective (NA = 1.2), an sCMOS camera for super-resolution imaging, a CCD camera for widefield fluorescence imaging, and 1000mW 488nm, 561nm, 640nm, and 750nm lasers. 647nm and 561nm excitation lasers were used at a 240mW power output, and the 405nm activation laser was used at 60mW.

The microscope was first calibrated using dual-color fluorescent beads. Calibration was done each day to obtain a point-spread function (PSF) that the software used as a benchmark for each blink during imaging. Upon calibration, the sample was inserted and the region of interest (the arcuate nucleus) was found based on the GHRH staining coupled to Alexa 488 using the widefield camera of the microscope. dSTORM images were then acquired on these GHRH cells and 10,000 frames were collected for each probe sequentially (Alexa 647 and Alexa 568) at 50 frames per second. 3 mouse brains from each condition were imaged (a total of 6 brains), 3 sections per brain, 3 images per section. As such, 27 images from each condition were imaged.

Electron microscope imaging

90 nm-thick sections on slotted TEM grids were imaged with the FEI Tecnai G2 Spirit BioTwin 120 kV Cryo-TEM, equipped with Gatan Ultrascan 4000 4k x 4k CCD Camera System, Model 895. Three brains were imaged, two from the trough of GH and

one from the peak of GH. To find the arcuate nucleus during imaging in the narrow field of view of an electron microscope, prior to sample preparation, the section was trimmed accordingly. At least eight images were acquired per section at magnifications ranging from 4,800x to 23,000x.

Focused Ion Beam-Scanning Electron Microscope (FIB-SEM) imaging

Sample blocks for analysis by FIB-SEM were prepared from the same block as in TEM. Each EPON block was trimmed and mounted on a 45° pre-titled SEM stub and coated with a 4 nm-thick of Pt to enhance electrical conductivity. Milling of serial sections and imaging of block face after each Z-slice was carried out with the Helios Nanolab 660 DualBeam using Auto Slice & View G3 version 1.5 software (FEI Company, Hillsboro, OR USA). A block was first imaged to determine the orientation relationship between the block face of ion and electron beams. A protective carbon layer 61 µm long, 7 µm wide and 2 µm thick was deposited on the surface of the region of interest to protect the resin volume from ion beam damaging and correct for stage and/or specimen drift, i.e., perpendicular to the image face of the volume to be milled. Trenches on both sides of the region were created to minimize re-deposition during the automated milling and imaging. Distinct imaging fiducials were generated for both ion beam and electron beam imaging and were used to dynamically correct for any drift in x and y during a run by applying appropriate SEM beam shifts. Milling was performed at 30 kV with an ion beam current of 2.5 nA, stage tilt of 6 degrees, a working distance of 4 mm. With each step, a 7 nm thickness of the material was removed with the ion beam. Each newly milled block face was imaged with a Through-the-Lens Detector (TLD) for backscattered electrons and In-Column-Detector (ICD) at an accelerating voltage of 2 kV, beam current of 0.4 nA, stage tilt of 44 degrees, and a working distance of 3 mm. The pixel resolution was 7.8 nm with a dwell time of 30 µs. Pixel dimensions of the recorded image were 1536 x 1024 pixels. One thousand images were collected and the contrast of the images was inverted.

dSTORM data analysis

All images were analyzed using the latest version of the SRX Vutara software (6.04.02) by Bruker. First, all blinking events captured during imaging were localized (or considered “real”) per specific parameters. As such, the “maximum frame accumulation” (or the maximum number of frames a fluorophore can persist across subsequent camera frames) was set to 10 frames. Above this number, a blink was considered a fiducial marker and used to correct for drift that might have occurred during imaging. The “cutout width” of a small region centered around the brightest pixel of a fluorophore was assessed visually and set to 16 pixels with a maximum of 1 emitter per cutout. The “maximum accumulation offset” (which represents the lateral offset in pixels that a given cutout’s brightest pixel can shift across sequential frames while still being considered the same fluorophore) was set to 4 pixels to avoid fluorophores across subsequent frames to be grouped as one single fluorophore. No maximum limit was set for the number of particles to be localized in a given frame and the background threshold was set to 30 for the 568 laser and 20 for the 647 laser. Next, since pre- and post-synaptic proteins form visually distinct clusters, cluster analysis was used to quantitatively assess various parameters of interest. These parameters included: the number of excitatory versus inhibitory clusters during peak and trough of GH secretion, the number of “functional synapses” that were defined based on the presence of both pre- and post-synaptic clusters for a particular synapse (if only the pre-synaptic cluster was present, that event was categorized as a “non-functional synapse” or “non-synaptic cluster”), the distance between pre-and post-synaptic clusters from center to center (the “centroid” distance). After localization, a DBScan algorithm (or Density-Based Spatial Clustering of Applications with Noise) was used to define and quantitatively assess clusters of pre-and post-synaptic terminals. DBScan finds core points that have dense neighbours and builds clusters from these points based on reachability so that all points in a cluster are density-connected (65). Two parameters must be set by the user: a minimum particle count to form a cluster and a maximum particle distance of a particle to be included in the cluster. For the former, due to the three-dimensional nature of images acquired on the Vutara microscope (biplane imaging), a minimum of 6 particles were chosen to form a cluster (2 in each coordinate: x,y,z). For the latter, a general rule was to select a parameter that stayed constant between individual clusters (in our case this was “Density”), then change the parameter of interest (maximum cluster distance) and plot a graph of maximum particle distance (x) versus density (y). Once no more particles could be reached with DBScan based on distance, the graph would start to “plateau”, i.e. the density of clusters will stop changing. The point of interest was then selected as the first point at which this “plateau” was observed. Once these parameters were set, a DBScan algorithm was run, the output saved to an Excel file and for more efficient synapse counting, an algorithm in the statistical software “R” was designed and used. To analyze the centroid distance between pre- and post-synaptic clusters, x,y and z positions of each pre-synaptic cluster were matched with x,y and z position of the corresponding post-synaptic cluster and the Euclidean equation was used for distance calculation ($\sqrt{(x_1 - x_2)^2 + (y_1 - y_2)^2 + (z_1 - z_2)^2}$).

Electron microscope and FIB data analysis

To quantify the FIB-SEM synaptic data, the image analysis program FIJI (Image J) was used. The FIB data was opened as a sequential image and analyzed using a single-blind protocol (a student who analyzed the data was not involved in the FIB image acquisition and therefore unaware of which samples the images came from). Using the Multi-point tool, each excitatory synapse and inhibitory synapse was labeled with a color-coded point. Each synapse was labeled a single time in all its z-slices. To determine what was an inhibitory synapse, the same criteria as in classical EM were used: we looked for symmetrical and thick cell membranes between a pre-synaptic cell (which has many vesicles, preferably docking) and a post-synaptic cell (which has no vesicles). They appeared this way throughout their z-coordinates. Identifying the excitatory synapse however was different. Initially, the same criteria were set as for classical EM: asymmetrical and thick membranes with the post-synaptic side being thickest. However, we quickly observed that there were no synapses that were asymmetrical the whole way through its z-coordinates. They appear to be inhibitory along its z-stack edges and become asymmetrical around the middle. As such, we had to modify our synapse-identification parameters to reflect this revelation. Excitatory synapses were labeled as green, inhibitory synapses as yellow, uncertain synapses as blue. Once the stack was labeled through, the program counted the amount of each color using the in-program counter.

To quantify the numbers of astrocytic processes, the same program (Image J) was used. Data was analyzed by two students independently who were trained in identifying astrocytes and neuronal tissue in general. Students were blind as to which condition was being analyzed. Brains from three mice were used: mouse 16 and 17 (trough of GH levels) and mouse 18 (peak of GH levels) and on average, 20 images per mouse were analyzed. Astrocytic process' were identified based on the presence of dense granules in their relatively bright cytoplasm, their stellate irregular shape and thin processes that extend in between membranes of axons, dendrites or somata (as described at www.synapseweb.clm.utexas.edu/astrocytes). If they did not display their granules in the plane of sectioning, they were identified as what is "left" when neuronal tissue is (visually) subtracted. Since images were acquired at multiple magnifications, data were normalized to the lowest magnification of 4800x (by multiplying the number of glia per μm^2 times the area of an image at 4,800x).

Statistical analysis

All statistical analysis was performed with one-way ANOVA combined with Tukey post-hoc Test

.

4. RESULTS

4.1 Plasma GH levels

A crucial task of our study involved obtaining tissue from mice that corresponded to a specific hormonal status of the animal. As such, we were interested in obtaining at least 3 brains from mice with high concentrations of GH measured from blood at the time of sacrifice/perfusion and 3 brains from mice with low GH concentration. Considering the timeline of experimental procedures (blood collection – perfusion and tissue collection – growth hormone measurement – tissue analysis), one can already see that the hormonal status of the mice was unknown at the time of perfusion. Therefore, to determine the time of sacrifice (and as such the time of the peak and trough of plasma GH levels in the mice) several approached were tested.

In the first approach (the “pilot experiment”), the times of the GH peak and trough were predicted based on what occured in rats in a previous study from our laboratory (7), with the first peak at 3 hours after “lights on” (~11:00) and the first trough two hours after the peak (~13:00). However, mouse GH profiles did not match those of rats and were also inconsistent and unpredictable among individuals (Fig.1A); therefore, another approach was implemented. In the second approach, blood collection from four mice was performed every 20 minutes starting at 09:20 and ending at 15:40, without sacrifice. On day two, plasma GH levels of all samples from the four mice were measured with ELISA. Based on individual GH concentration profiles of each mouse, the time of sacrifice of each mouse to obtain two brain tissue samples from the peak and two brain tissue samples from the trough of GH secretion was predicted (Fig.1B).

On day three, blood collection (every 20 minutes) was performed again from the same four mice (another tail-clip excision was necessary) and each mouse was sacrificed based on the predicted time from day one of blood collection. However, profiles of day three did not match those of day one and therefore only one brain tissue sample was obtained from the peak and three brain tissue samples from the trough (Fig.1C). Finally, since it was difficult to predict the exact timing of GH peak or trough in individual mice, the time of sacrifice was chosen randomly. Based on the full 6-hour collection profiles from day one, there was at least a 25% chance of perfusing the mouse at its peak (since the duration of the peak period was one hour and the time from peak to peak was approximately four hours). This was the method used for subsequent perfusion times. A total of 18 mice were perfused, 14 for super-resolution imaging and 4 for electron microscopy and FIB (Fig. 1D). Out of 14 brains obtained for super-resolution imaging, 2 were not considered in the analysis (mouse 4,8) due to the lack of discernable GH profile at the time of sacrifice (mice were perhaps not fully habituated and therefore stressed; see more in Discussion), 5 brains were collected at the peak (mouse 6,9,11,13,14) and 7 at the trough (mouse 1,2,3,5,7,10,12). Three mice brains from the peak period (mouse 6,9,13) and three brains from the trough period (mouse 1,3,5) were used for dSTORM imaging and analysis. Out of the four brains obtained for electron microscopy and FIB analysis, one brain was collected at the peak (mouse 18) and three brains at the trough (mouse 15,16,17). One brain from the peak (mouse 18) and two brains from the trough (mouse 16,17) were used for subsequent EM imaging and analysis and one brain of each for FIB-SEM analysis (mouse 17,18).

4.2 Optimization of dSTORM staining and tissue preparation

Although a protocol for dSTORM imaging developed by a previous graduate student (Steven SIlvestrin) already existed in the lab, due to availability of a new antibody that was not previously used (GHRH from AbClonal), new protocols for buffers, and the availability of improved software imaging and analysis tools, the protocol was revisited (summarized in Table 1).

The first task was to find a suitable antibody that could specifically stain GHRH neurons. This has been a daunting task for our lab in the past, as labeling this parvocellular hormone in neuronal cell bodies proved to be difficult due to its low concentrations in the cytoplasm; as such, the staining was always unsatisfactory (weak and not very specific). However, a new GHRH antibody by ABClonal was released on the market recently (A5343 GHRH, polyclonal). Various dilutions of the new antibody were initially tested (data not shown) and 1:500 was ideal. Moreover, the staining was also specific to the arcuate nucleus and the median eminence (high concentrations of GHRH are mainly found in these two brain regions, with very high concentrations in the median eminence, a site of GHRH accumulation and release) (Fig.2, top image). GHRH was labeled with an Alexa 488 antibody and visualized with a widefield camera on the the Vutara dSTORM microscope (Fig. 2, bottom image).

Moreover, the image quality of dSTORM relies heavily on the efficacy of “blinking” (the “on” and “off” states of fluorophores). This efficacy is evaluated mostly by brightness and the fraction of molecules in the “on” state. However, different dyes blink best in different buffers and when considering a sample with two or three labels, optimal blinking can become quite challenging. As such, a new buffer (“OxEA”) that relies on Oxyrase Oxygen-scavenging system that should not acidify the medium upon consuming O_2 was tested (65). However, when compared to the Gloxy-MEA-Mercaptoethanol buffer that was previously used by our lab, no notable difference was found in the longevity of the buffer; the time of imaging before the “blinking” efficacy decreased was approximately the same for both buffers (~1 hour). Therefore, we decided to continue using the original Gloxy-MEA-Mercaptoethanol already acquired by our lab. However, we decided to tightly control the pH of the Gloxy-MEA-Mercaptoethanol imaging buffer to improve the efficacy of blinking and signal-to-noise ratio (with a slightly higher pH, the blinking was reduced) (data not shown). Therefore, with every new preparation of the buffer, the buffer was adjusted to pH 8 with NaOH.

To prevent drift during imaging, tissue was left to dry overnight on a coverslip to attach itself properly to the glass surface. However, when rehydrated the next day with the blinking buffer and layered with a second coverslip, due to tissue expansion, we noticed significant drift during the first 10-minute acquisition period. This was puzzling at first, however when the tissue was left to re-hydrate with the buffer for 5-7 minutes before imaging, the drift was halted (data not shown).

Lastly, to obtain a higher image quality, we decided to acquire 10,000 frames instead of the 2,000 previously used and only over 1 cycle (instead of 5). With many cycles of imaging going through the tissue repeatedly, the fluorophores bleached faster and by acquiring more frames with less cycles, it was possible to limit bleaching and obtain better signal-to-noise ratio (data not shown).

4.3 Synaptic and non-synaptic cluster populations

With this project, our goal was to visualize pre- and post-synaptic markers of inhibitory and excitatory synapses at super-resolution to extract quantitative information about the size and numbers of synaptic clusters under high and low GH concentrations in mice. As such, Gephyrin and VGAT as well as VGLUT2 and PSD95 were initially stained and imaged under a confocal Zeiss LSM 710 microscope with a 63x/NA 1.4 oil immersion objective and then with Vutara dSTORM equipped with a 100x/NA 1.2 water immersion objective to compare and understand the limits and advantages of both microscopic approaches.

Three 30 µm tissue sections from a random mouse (without a defined GH profile) were stained with antibodies against Gephyrin and VGAT or VGLUT and PSD95 as described in Materials and Methods. Anti-VGAT or anti-VGLUT2 was then paired with Alexa 647 and anti-Gephyrin or anti-PSD95 with CF 568 as fluorophores for dSTORM imaging. For confocal microscopy, the same pairs of primary antibodies were similarly labeled with secondary antibodies conjugated to Alexa 488 and Alexa 647, respectively. When imaged with the confocal microscope, VGLUT2 and PSD95 were found in dense clusters (Fig.3) (VGAT and Gephyrin data not shown). dSTORM allows visualization of these clusters at a better resolution and measurement of their volumes with high precision (lateral resolution ~30 nm).

As such, when cluster analysis was performed on dSTORM images (as described in Materials and Methods), the surface area of most clusters was in the range of 0.01 to 0.15 µm^2. Interestingly, additional population of clusters below 0.01 µm^2 was found that was not visible in the confocal image (Fig. 3, top image). Moreover, it was found that clusters below 0.01 μm^2 were not “paired” (i.e. a pre-synaptic cluster did not pair with a post-synaptic cluster and vice versa). Most clusters in the range of 0.01 to 0.15 μm^2 had their pre- or post-synaptic partners. As such, since a synapse should consist of a pre- and post-synaptic membrane with its dense clusters, clusters below 0.01 μm^2 were considered “non-synaptic” cluster populations.

4.4 Synapse numbers during peaks and troughs of GH secretion

To understand how synaptic connectivity changes during the ultradian pattern of GH secretion, dSTORM imaging of inhibitory and excitatory synapses was used to count their numbers during both profiles of GH secretion. The minimum number of particles to form a cluster was set to 6 and a particle distance was set for each image (as described in Materials and Methods). Three tissues from three mice were imaged for both conditions, for both synapse types. No limit was set as to the surface area of a cluster; however, a synapse was defined as a cluster of pre-and post-synaptic markers that are no further than 100 nm apart (67). To count synapses, multiple dSTORM data sets (6-10 per mouse) were analyzed, synapse numbers were extracted through cluster analysis in the Vutara SRX software, and data was organized and classified in an in-house build plugin for the “R” statistical software. To account for synapse variability between the different mouse brains, synapse numbers are reported as ratios of inhibitory to excitatory synapses (instead of absolute synapse numbers). Only synapses contacting GHRH neurons were considered (as described in Materials and Methods) by widefield overlay of GHRH staining with pre- and post-synaptic markers.

We found that during troughs of GH levels, 66% of all synapses were inhibitory and 34% were excitatory. During peaks of GH levels, 71% of all synapses were excitatory and 29% were inhibitory (Fig. 4). There was a significant difference between the number of excitatory synapses during GH trough and inhibitory synapses during GH peak. As such, there was an ultradian change in the number of synapses in parallel with the ultradian change in GH levels; when hormone levels were low (GH cells were not stimulated), GHRH cells received more inhibitory input. When hormone levels were high (GH cells were stimulated), GHRH received more excitatory input.

4.5 Numbers of synaptic versus non-synaptic clusters

In line with previous findings, where more inhibitory synapses were found during low GH levels and more excitatory synapses were found during high GH levels, we wanted to evaluate whether these changes in synapse numbers are due to the mobilization of free non-synaptic clusters that associate together to form a functional synapse (it is known that synapses are formed from smaller clusters that associate together in a step-wise manner; see more in Discussion) (68).

Therefore, since we showed before that non-synaptic cluster populations below 0.01 μm^2 can be visualized with dSTORM, we wanted to compare the number of synaptic to non-synaptic clusters under both profiles of GH secretion. Again, cluster parameters were set as described in Materials and Methods and a synapse was defined based on the proximity of the pre-synaptic cluster to its post-synaptic cluster partner. On average, ~80-100 clusters were analyzed per image, 6-10 images were analyzed per tissue section. Three tissue sections were imaged per mouse and three mice were used for one GH condition (so that a total of ~4320-9000 clusters were analyzed for trough- and the same for peak of GH levels).

We found that during troughs of GH levels, 58% of all inhibitory pre-synaptic clusters were associated with inhibitory post-synaptic clusters (58% were “functional synapses” and 42% were non-synaptic clusters) and 41% of all excitatory pre-synaptic clusters were associated with excitatory post-synaptic clusters (59% were non-synaptic) (Fig. 5). During peaks of GH levels, 65% of all inhibitory pre-synaptic clusters were associated with inhibitory post-synaptic clusters (35% were non-synaptic) and 81% of all excitatory pre-synaptic clusters were associated with excitatory post-synaptic clusters (19% were non-synaptic) (Fig.5). As such, there was a significant difference in the percent of excitatory “functional” synaptic clusters - 41% during troughs vs 81% during peaks. This potentially indicates a mobilization of non-synaptic cluster populations during peaks of GH levels. Moreover, this difference was not observed for inhibitory synapses - 58% of “functional” synaptic clusters during troughs of GH levels as compared to 65% during peaks of GH levels.

4.6 Pre- to post- synaptic cluster distance

Next, we wanted to understand whether there is any change in the distance between pre-and post-synaptic clusters. Our initial rationale was that, if astrocytic processes interrupt synaptic transmission or synapse formation by inserting themselves between neuronal membranes and potentially mobilize free synaptic clusters to form synapses during excitation, we might be able to detect an increase in the distance between pre-and post-synaptic clusters during troughs of GH levels (astrocytic processes are wider than the size of the synaptic cleft [>40 nm]). Only synaptic clusters were considered based on their pre-to post-synapse proximity (non-synaptic cluster populations were eliminated from the analysis via an in-house built plugin for the “R” software).

We found no significant difference between the centroid distance of clusters in both GH secretion profiles (Fig. 6). On average, the distance between pre-and post-synaptic clusters during troughs of GH levels was 341 nm, and 351 nm during peaks of GH levels. This distance was consistent across ~1000-2000 clusters. Therefore, the distance between pre- and post-synaptic markers does not change between troughs and peaks of GH secretion; as such, astrocytic processes do not appear to widen the distance between pre- and post-synaptic clusters during low levels of GH secretion.

4.7 Electron Microscopy and Focused Ion Beam analysis - astrocytic processes

Since we did not find differences in distances of pre- and post-synaptic terminals during our dSTORM analysis, we wanted to understand the tissue context better between the two phases of GH secretion. For this reason, we resorted to transmission electron microscopy (TEM) and focused-ion beam scanning electron microscopy (FIB-SEM). Two mice from the trough of GH levels and one mouse from the peak of GH secretion were chosen and 90 nm-sections imaged with an electron microscope. No immunogold staining was performed since our interest was only to compare the tissue context of both GH profiles. Lack of permeabilization also allowed us to fully preserve membranes. Upon imaging by electron microscopy at magnifications starting from 4800x, we observed multiple astrocytic processes intertwined between neuronal membranes during the trough of GH secretion (Fig.7). We also noticed some during the peak of GH secretion (Fig.8). We also observed that the location of astrocytic processes during troughs of GH secretion was often such that a potential synapse could have formed if the astrocyte was not there (in between membranes with pre-synaptic vesicles and a post-synaptic dendrite or a potential axo-axonic synapse with both neurons filled with synaptic vesicles). To quantify the numbers of astrocytic processes present in between neuronal membranes, multiple parameters were set as described in Materials and Methods. Upon quantifying numbers of astrocytes present in both conditions and normalizing the data to a magnification of 4,800x, on average, 4.4 astrocytic processes were found in between neuronal membranes during troughs of GH levels and 1.8 astrocytic process during peaks of GH levels (which represents 0.48 and 0.019 astrocytic process per um^2 of tissue during troughs and peaks, respectively). As such, more than twice as many astrocytic processes associate between neuronal membranes where potential synapses could form during the trough of GH secretion than during the peak of GH secretion. Moreover, no astrocytic processes were found between pre-and post-synaptic terminals directly (synapses are easily identified in electron microscopy images as symmetric (inhibitory) or asymmetric (excitatory) black membrane “thickenings”). This was in line with our results from dSTORM analysis, where no difference was found in the distance between pre-and post-synaptic terminals. Once TEM was performed, we wanted to visualize astrocytic processes in 3D with FIB-SEM to confirm their presence in between neuronal membranes; as with any 2D analysis, there is always a chance of an error based on the plane of sectioning or inaccurate interpolation of what is seen in one image to the entire structure of interest. As such, two FIB-SEM images were acquired; one from the brain section of a mouse perfused at the trough of GH secretion (mouse 17) and one from the peak (mouse 18). A video was compiled, which represents a series of images from the brain of mouse 17. In the video (not shown), 7 nm of tissue is visualized in 3D and few astrocytic processes can be followed. These processes, as expected, are intertwined in areas where possible synapses could form but also in between neuronal membranes and brain tissue in general. More astrocytic processes in spaces where potential synapses could form were present in mouse 17 as compared to mouse 18 (at least four astrocytes could be followed in mouse 17 and only one in mouse 18). We also tried quantitatively assess numbers of synapses through FIB to confirm our findings from dSTORM analysis, as FIB would provide us with an unbiased estimate of synapse numbers (see more in Materials and Methods). However, the task proved to be more difficult than expected and results obtained from two independent observers were very different, where for example, one observer reported more inhibitory synapses during GH trough and the other reported the opposite (for the reasoning behind the difficulty of such analysis, see Discussion). As such, these inconclusive results were not included in this report.

5. DISCUSSION

In this study, we used super-resolution dSTORM imaging, transmission electron microscopy (TEM) and focused ion-beam scanning electron microscopy (FIB-SEM) to better understand the mechanism behind ultradian changes in synaptic connectivity that are known to occur in parallel with the ultradian pattern of growth hormone secretion.

dSTORM imaging and analysis allowed us to quantify the number of inhibitory and excitatory synapses, measure cluster density and centroid distance from pre- to post-synaptic clusters of inhibitory and excitatory synapses. TEM allowed us to obtain insights into the tissue context of synapses during low and high levels of GH and to quantify the number of astrocytic processes that associate with neuronal membranes. Lastly, FIB-SEM was used to visualize astrocytic processes in 3D. We found more inhibitory synapses during troughs of GH and more excitatory synapses during peaks of GH. We also found that more pre-synaptic clusters associate with post-synaptic clusters during peaks of GH. Lastly, we found no difference in the centroid distance of pre-to post-synaptic clusters in dSTORM, which was confirmed by TEM and FIB-SEM, where astrocytic processes were found in between neurons but not directly between synapses. Lastly, more astrocytic processes were found between neuronal membranes during troughs of GH as compared to peaks of GH.

Eighteen mice were perfused in total and their brain tissue was used for dSTORM, TEM and FIB-SEM analysis. Obtaining tissue that precisely corresponded to the trough or peak of GH secretion proved to be challenging. The experimenter had to be quick to ensure that the mouse is perfused as soon as possible after the blood collection, so that the state of the tissue closely corresponded to the state of the GH level in blood. Blood collection lasted for approximately 30 seconds, injection and perfusion took no more than 15 minutes. Therefore, a maximum delay between blood collection and perfusion was around 16 minutes. Considering that the shortest peak period in mouse 7 and mouse 17 lasted for about 30 minutes (troughs were much longer), in theory, if the blood was measured exactly in the middle of the peak period and the delay in collecting the tissue was 16 minutes, there was a chance that the blood measurement corresponded to the peak of GH but the state of the tissue to the trough of GH secretion. This would have been problematic for all mice perfused during peaks. However, all mice that were perfused at the peak of GH secretion in this project were in the ascending phase of the peak, therefore having more than 16 minutes to remain in the peak period before tissue collection, even if the peak was very short, as in mouse 7 and 17 (~30 minutes).

Second, the absolute levels of GH (in ng/ml) varied between mice. There were mice perfused at the peak whose absolute value of the GH was low (ex. mouse 11, “peak” value at around 0.8ng/ml) as compared to mice perfused at the trough whose absolute value of the GH was higher or equal (ex. mouse 12, “trough” value at around 0.9 ng/ml). However, this was not worrisome, since the absolute concentrations of hormones should be specific to each individual mouse, yet what mattered was the GH secretion pattern in each individual animal to infer the timing of peak and trough.

Moreover, despite the recommended two-week habituation starting in our second round of experiments (mouse 3 onwards), some mice still seemed not fully habituated. Although stress was not observed with the “naked eye” during the blood collection period (all mice were active with normal eating habits, did not defecate nor urinate), it was displayed as “flat lines” of GH concentrations at each time point in Fig.1A. Stress specifically inhibits the periodic pattern of GH secretion (and less the absolute values of GH concentration). As such, mice with “flat” GH profiles were not included in the final analysis (mouse 8).

Pre- and post-synaptic proteins associate in clusters, therefore it was not surprising to see clusters of Gephyrin and VGAT as well as VGLUT2 and PSD95 in dSTORM. What was novel, was to see pre-synaptic clusters below the surface area of 0.01 μm^2 that were not associated with synapses. This made sense however, considering the mechanism behind synapse formation (68). Pre-synaptic membranes consist of synaptic vesicles that are transported anterogradely towards the active zone to form clusters. At rest and low rates of stimulation, most of the vesicles composing this pool remain in a tight cluster. They are actively utilized when neurons fire action potentials at higher rates and the capability of the recycling machinery is limited. In addition, synaptic vesicle clusters can migrate between release sites and reassemble into clusters between sites, thus creating quick “cluster plasticity” (68). Considering that we used VGLUT as a marker of pre-synaptic membranes (which labels vesicles containing GLUT receptors), observing small clusters below 0.01 μm^2 perhaps reflected this phenomenon.

In our study, more pre-synaptic clusters associated with post-synaptic partners during peaks of GH than during troughs of GH secretion. One explanation for this could be that during peaks of GH, there is some sort of mobilization of free pre-synaptic clusters to form the active zone. This could also explain the observed increase in the numbers of excitatory synapses during peaks of GH. However, the mechanism behind this phenomenon is unknown and here is only based on speculation. Since it is known that glial cells secrete multiple gliotransmitters to drive various processes at the synapse (as described in the Introduction), it is possible that a signal exists which would, perhaps through neuronal receptor signaling, induce calcium influx into the pre-synaptic membrane and cause free cluster mobilization. However, this is yet to be investigated.

Our initial hypothesis was that we would see more astrocytic processes between synapses directly (however, this was not the case as described in Results). To investigate this, we had to establish a rigid method that would allow us to accurately measure the distance between pre- and post-synaptic clusters (if an astrocytic process invades the synaptic cleft, due to its size, it would widen the cleft size and this would be observed as an increase in the distance between pre- and post-synaptic membranes). One method was to measure the *minimum inter-cluster distance* (in essence, the size of the synaptic cleft). However, since the SRX software associated with the dSTORM microscope makes the measurement based on the distance of two particles only (the closest particles to capture the minimal inter-cluster distance), this did not seem like a rigid, statistically sound method for claiming the true distance between clusters as wholes (as any potential “noise” particle that is in close proximity to another particle could be potentially considered by the software). Therefore, the distance that was chosen was from the center of mass of a pre-synaptic cluster to the center of mass of a post-synaptic cluster (centroid to centroid) as described in Materials and Methods. The fact that this method was accurate was validated with EM imaging; we did not find any astrocytic processes directly between synapses in EM images, but rather in between neuronal membranes (we also did not find any difference in centroid distance between pre- and post-synaptic clusters with dSTORM).

Moreover, we also aimed to use FIB-SEM data analysis to count the number of synapses. This would provide us with an unbiased estimate of total numbers of inhibitory vs. excitatory synapses during peaks and troughs of GH levels (unbiased, since the observer does not “see” into the tissue before image acquisition). However, this type of analysis proved to be difficult. Two independent observers obtained two very different results that were in opposition to one another. This was most likely due to the fact, that some synapses that were initially seen as inhibitory (symmetric pre- and post-synaptic membranes), “became” excitatory deeper into the tissue (parts of membranes would thicken, creating an asymmetric post-synaptic density) and then became symmetric again. This was very puzzling, leading us to question where a synapse starts and ends, and what kind of a synapse it is. It was *not* possible that the “thickening” was reflective of the post-synaptic asymmetric density while the symmetric part was only a pre- and post-synaptic membrane with receptors earlier or later in the tissue, since the pre-synaptic membrane should have the same length as the post-synaptic density (~50 nm) (25). This was most likely due to the plane of sectioning with the FIB beam relative to the synapse orientation and could not have been avoided. Moreover, it was difficult to notice once a new synapse “appeared” among the 1000 images analyzed. Often, synapses would be double-counted or not counted at all. As such, due to these encountered difficulties, we decided to halt such analysis using FIB-SEM data.

In the future, we would like to acquire more animal tissue to increase the sample size for the TEM analysis of astrocytic processes. Out of the four animals perfused for TEM, we only obtained one brain tissue during a peak. It is difficult to be certain that what is seen in a mouse with regards to astrocytic processes coverage of neurons will also be seen in a population. At minimum, two additional mice should be collected at the peak and one additional at the trough of GH secretion. In addition, we would like to perform astrocyte segmentation using our FIB-SEM data. In this way, we could graphically “extract” a full astrocyte and its processes as a visual representation in 3D to confirm that it is indeed an astrocyte and to indicate its localization in between neuronal membranes. Lastly, it would be interesting to investigate further the cluster mobilization as a potential mechanism behind increased numbers of excitatory synapses during peak and more pre-synaptic cluster association with post-synaptic partners during peaks of GH secretion.

6. FINAL CONCLUSIONS

All in all, in this project we quantitatively assessed synaptic data during two hormonal profiles of mice: troughs and peaks of GH levels using dSTORM, TEM and FIB-SEM. We found differences in synapse numbers, with more excitatory synapses during peaks of GH levels and more inhibitory synapses during troughs of GH levels. Moreover, we found a correlation between the hormonal status of the mice and the astrocytic coverage of neuronal membranes, with low levels of GH having more astrocytic processes intertwined in between neuronal membranes. Lastly, we found that there could be a potential mobilization of free pre-synaptic clusters during peaks of GH to drive excitation. Our data sheds light on the potential mechanism behind the ultradian changes in synaptic connectivity that occur in parallel with the ultradian rhythm of GH secretion. The importance of this study was to add to the pool of knowledge in the neurosciences, perfect the dSTORM technique and showcase yet another of its applications in biology. This, hopefully, will guide future scientists to more discoveries with regards to ultradian patterns of hormone secretion as well as further evolution of dSTORM and super-resolution microscopy in general.

7. FIGURES AND TABLES

Fig 1A. Mouse GH profiles do not match those of rats.

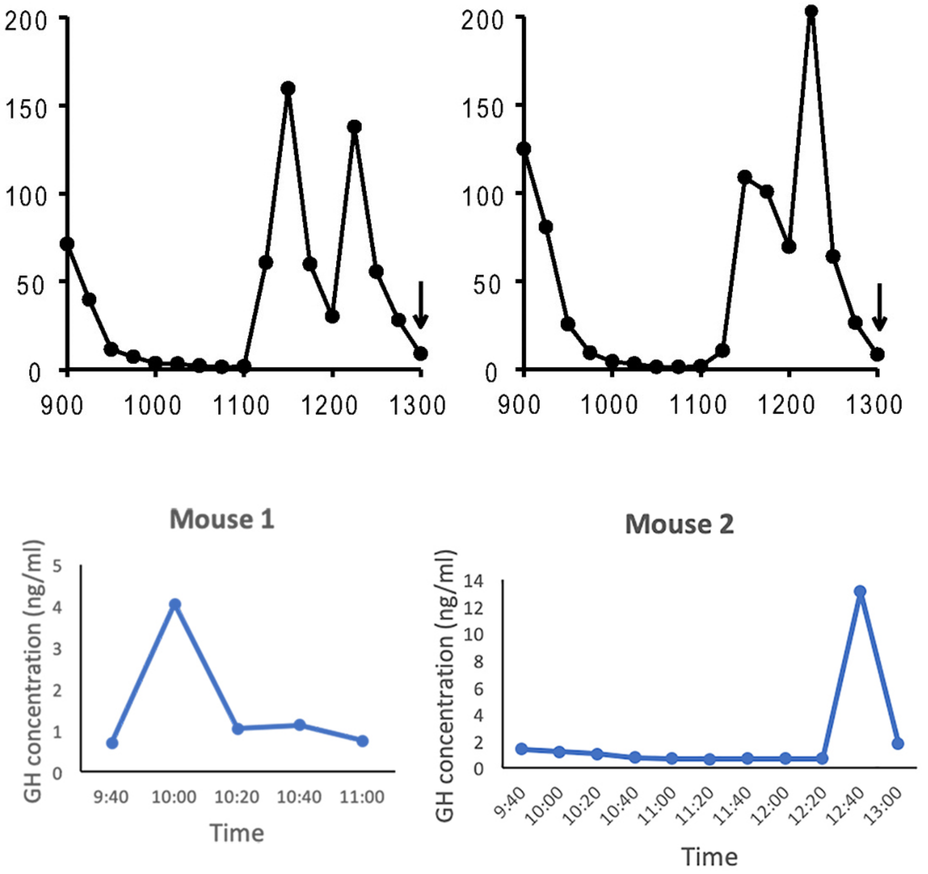

Fig. 1A. Growth hormone profiles of rats (top panel)* and mice (bottom panel). Whereas rats exhibit a predictable peak of GH secretion at 11:00 (top left image) and a trough at 13:00 (top right image), this was not the same in mice (bottom left and right). When mice were perfused at 11:00 and 13:00, both were in their trough of GH secretion.

*Top panel reproduced with the permission of the Journal of Neuroscience from Stroh *et. al*, 2009.

Fig 1B. 6-hour collection profiles of mouse GH.

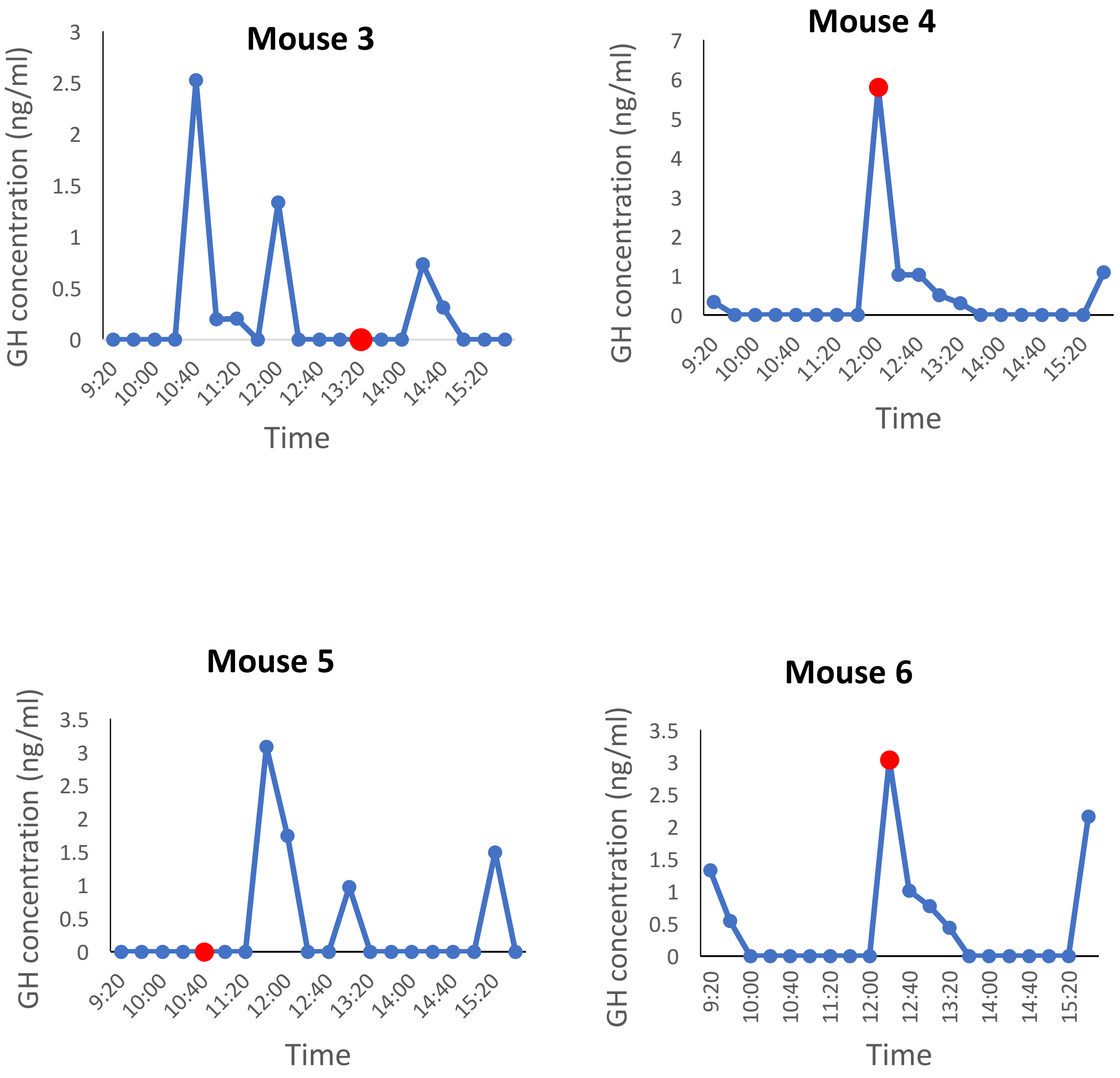

Fig. 1B. 6-hour individual GH profiles of four different mice on day one. Based on these profiles, perfusion times were selected (for day three perfusion) so that two mice (mouse 3 and 5) are perfused at their troughs and two at their peaks (mouse 4 and 6) of GH levels. Red dots represent perfusion times that were chosen.

Fig. 1C. Profiles of mice from Fig. 1B. at the time of perfusion.

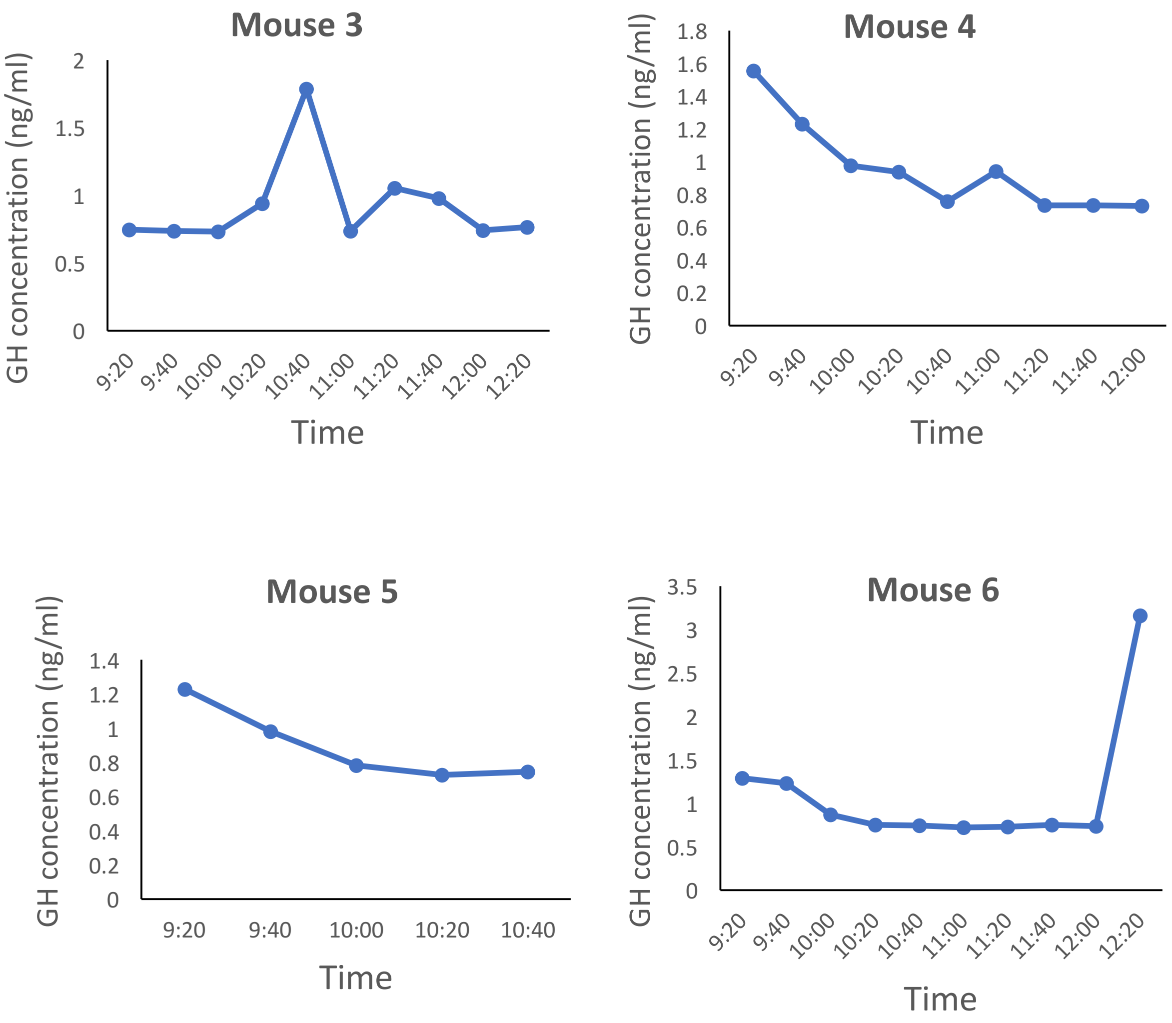

Fig. 1C. Day three perfusions of the same four mice as in Fig. 1B. GH levels at the time of perfusion did not match those established on day 1 during a 6-hour blood collection (Fig. 1B). As such, three mice (mouse 3,4,5) were perfused at their troughs of GH secretion (at 12:20, 12:00,10:40, respectively) and one mouse (mouse 6) at its peak of GH secretion (at 12:20).

Fig. 1D. Profiles of mice perfused at random hours.

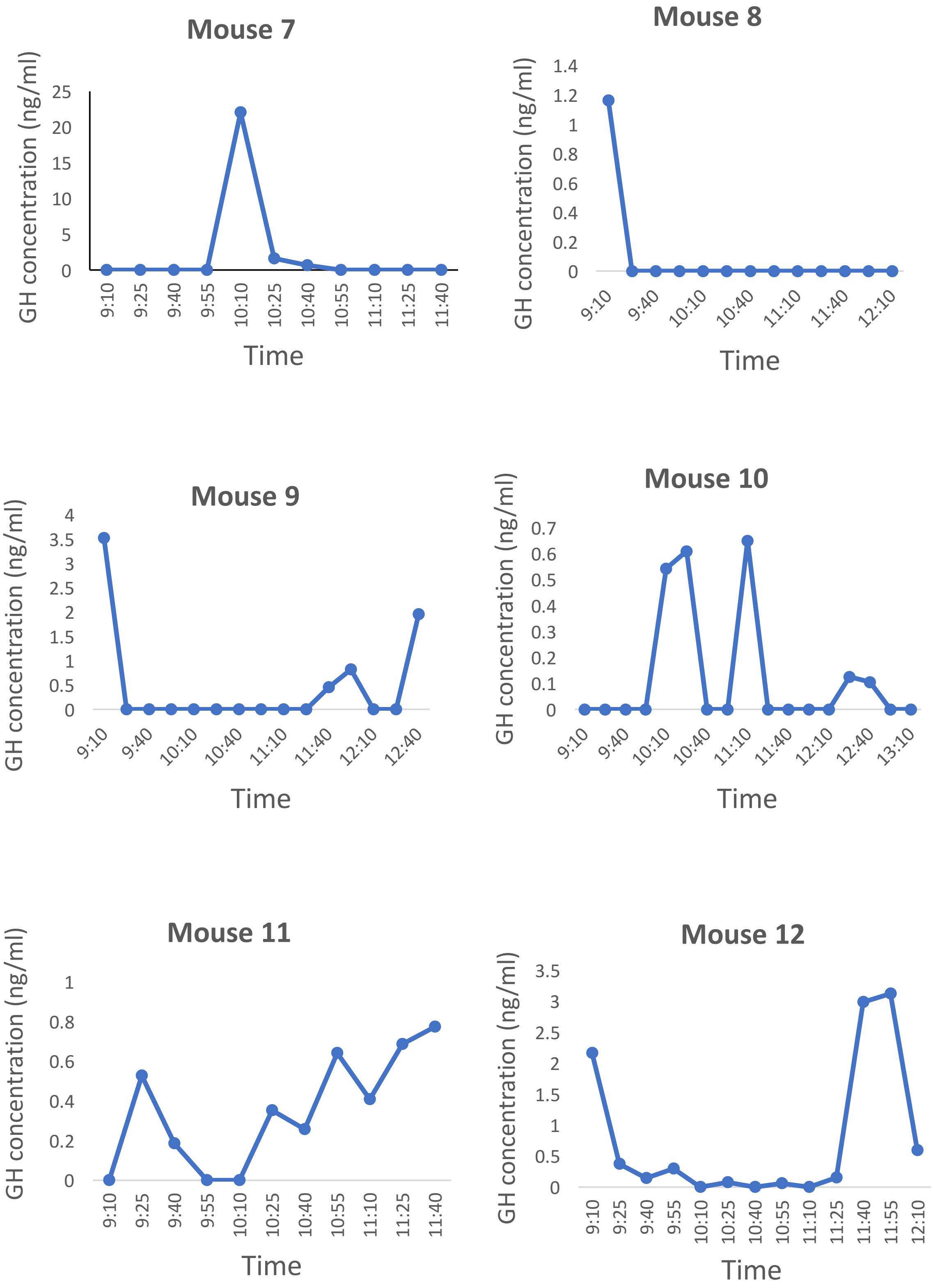

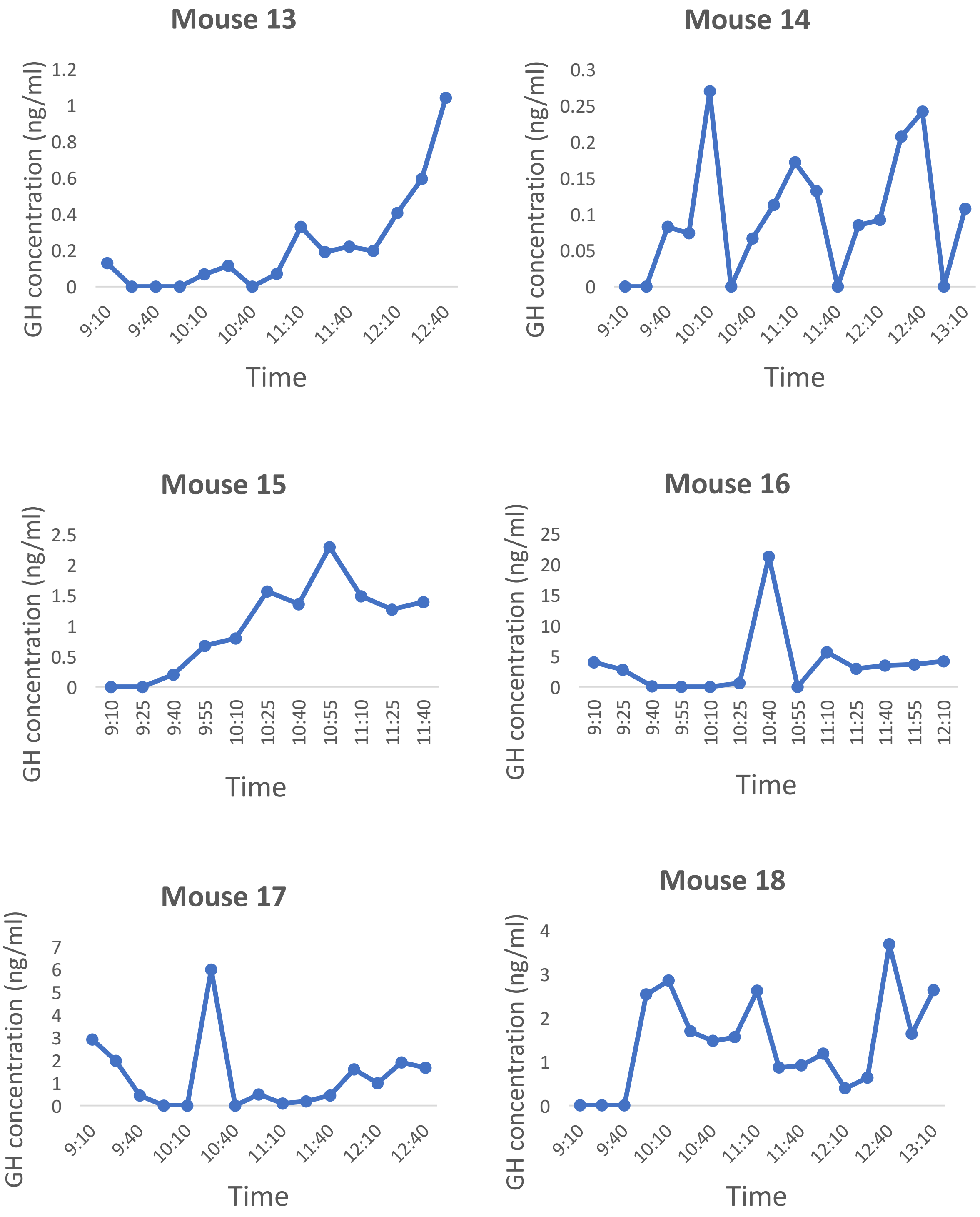

Fig. 1D. Profiles of the remaining mice that were perfused at random times. Mice 7-14 were perfused for dSTORM and mice 15-18 for TEM and FIB-SEM. Mouse 8 was excluded from the final analysis due to a prolonged lack of discernable GH rhythm ("flat" GH levels for ~3 hours).

Fig 2. GHRH immunofluorescence is specific to the arcuate nucleus and the median eminence.

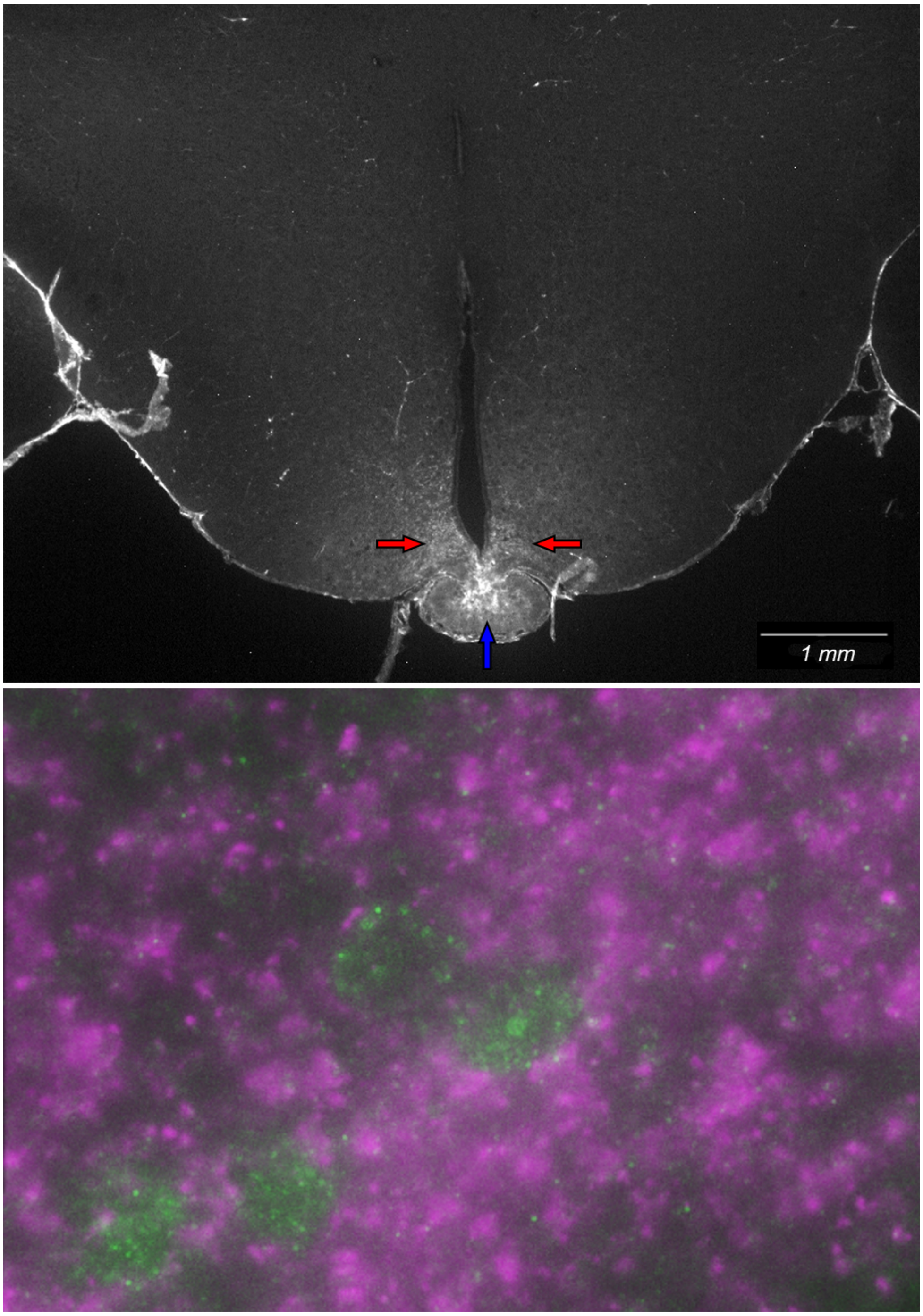

Fig.2. *Top image*: Mouse brain labeled with a GHRH antibody (visualized with Alexa 488 on a Nikon widefield microscope). Red arrows point to the arcuate nucleus and the blue arrow points to the median eminence, where the staining is the strongest. Only the lower part of the brain is shown (lowest zoom available).

Bottom image: A widefield image of GHRH immunofluorescence staining (green) and Gephyrin staining (magenta). GHRH localizes mainly to the cytoplasm while Gephyrin clusters surround cell membranes and are excluded from the cytoplasm.

Fig. 3. Clusters of pre- and post-synaptic proteins.

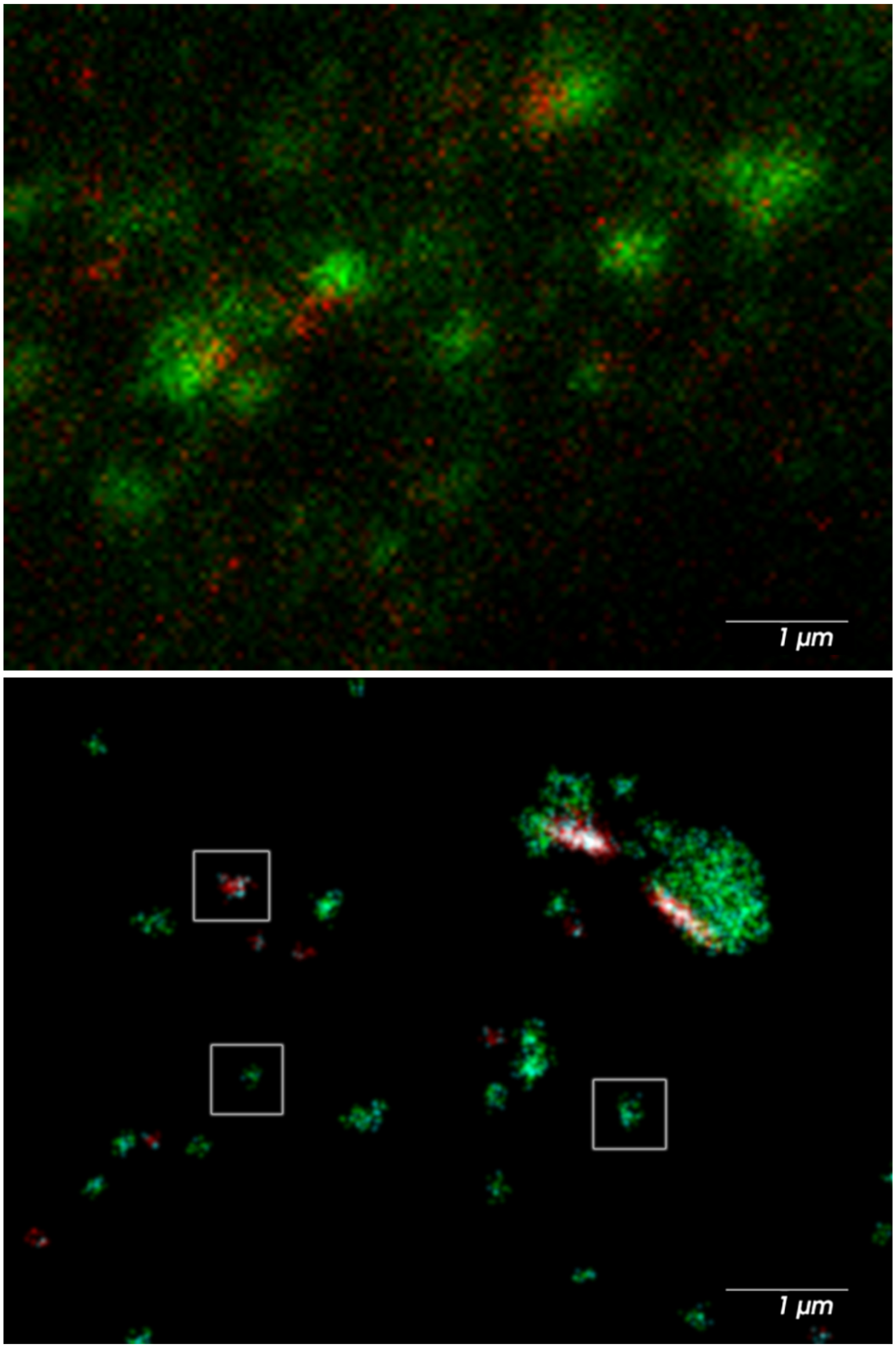

Fig. 3. Clusters of VGLUT2 (green) and PSD95 (red) imaged via Zeiss confocal microscope equipped with 63x oil immersion lens (top image) and Vutara dSTORM microscope equipped

with 100x water immersion. Additional non-synaptic cluster population below a surface area of 0.01 um^2 was visualized with dSTORM (bottom image highlighted in squares).

Fig. 4. Numbers of inhibitory and excitatory synapses during troughs and peaks of GH secretion.

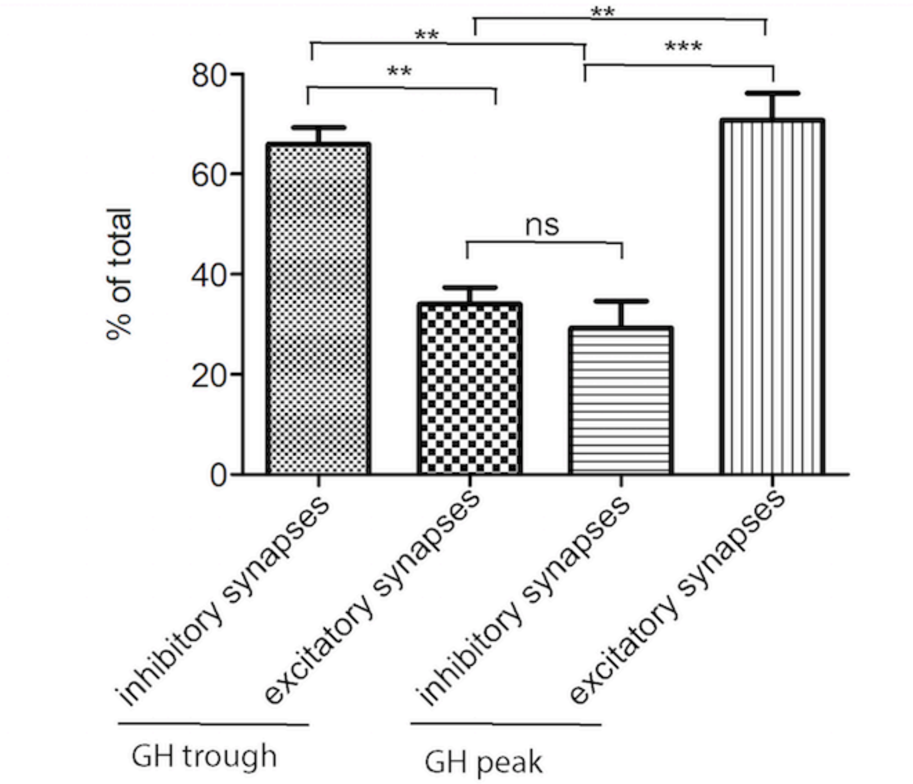

Fig. 4. Percent of inhibitory and excitatory synapses during GH troughs and peaks. During GH troughs, 66% of all synapses are inhibitory and 34% excitatory. During GH peak, 71% of all synapses are excitatory and 29% inhibitory.

Fig. 5. Percent of pre-synaptic clusters associated with post-synaptic clusters

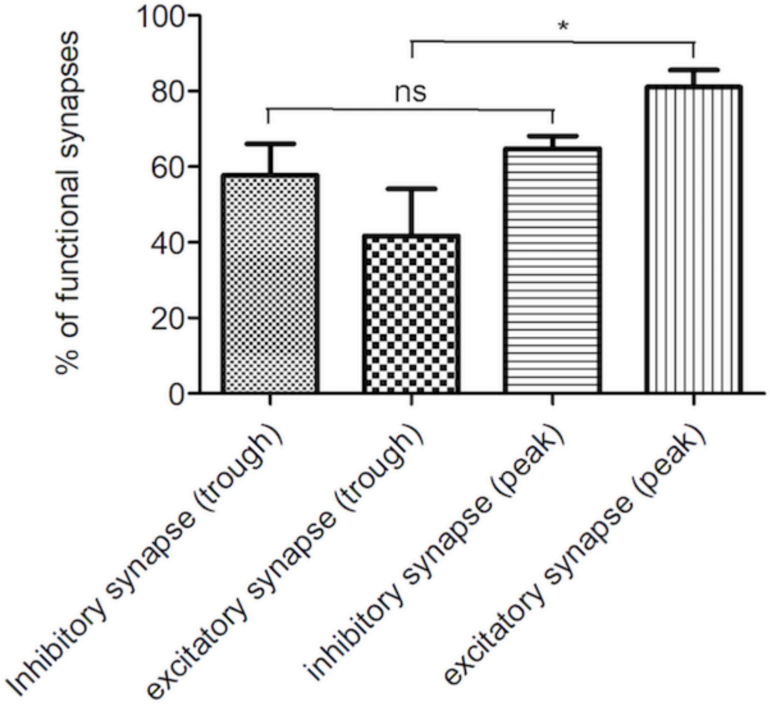

Fig. 5. Percent of pre-synaptic clusters that associate with post-synaptic clusters to form a "functional synapse" during peaks and troughs of GH secretion. There is a significant difference in the percentage of pre-synaptic excitatory VGLUT2 clusters that associate with post-synaptic excitatory PSD95 clusters between GH peaks and troughs (41% "functional synapses" during troughs as compared to 81% "functional" synapses during peaks).

Fig. 6. Centroid distance of excitatory and inhibitory synaptic clusters

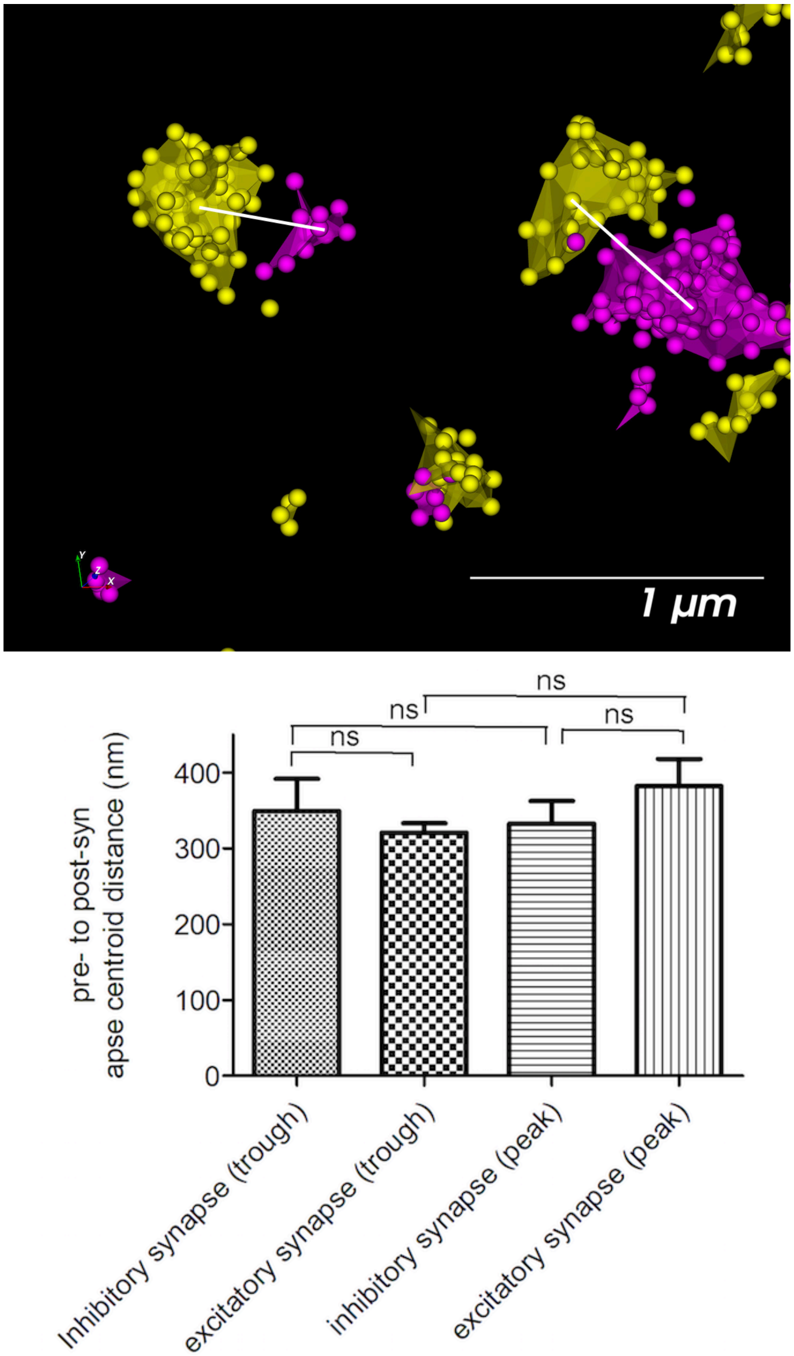

Fig. 6 “Centroid” distance of pre- and post-synaptic clusters during peaks and troughs of GH secretion as measured with the Vutara SRX software (top image; pre-synapse in pink, post-synapse in yellow). There was no significant difference in the centroid distance between peaks and troughs of GH secretion and on average, the distance was ~340 nm for GH trough and ~350 nm for GH peak (bottom graph).

Fig. 7 Electron microscope image of a mouse brain during a trough of GH secretion.

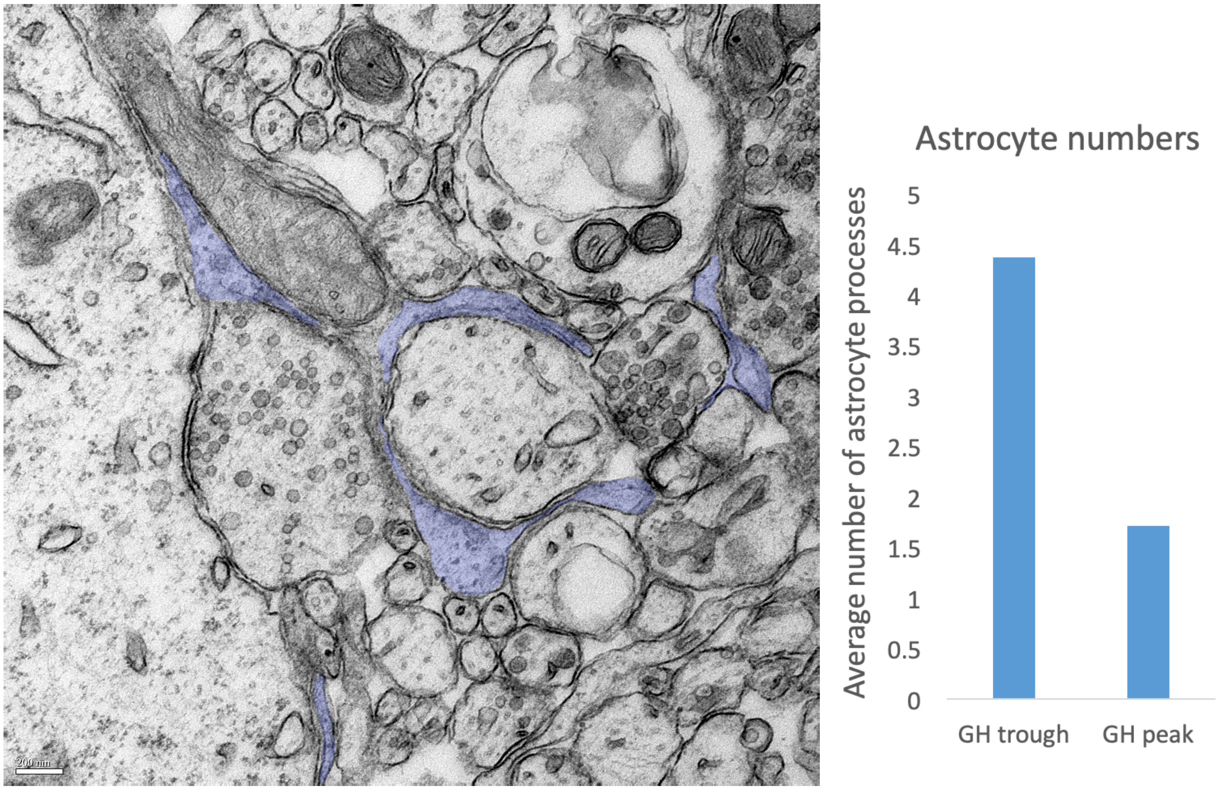

Fig. 7. Electron micrograph of a mouse brain perfused during a trough of GH secretion (left). Multiple astrocytic projections are demarcated in blue. Quantification of astrocytic processes during GH troughs and GH peaks (right). The average number of astrocytic processes per image at a magnification of 4,800x during GH troughs was 4.4 and during GH peaks 1.8. On average, 20 images were quantified from two mice for GH troughs and 20 images for GH peaks from one mouse.

Fig. 8. FIB-SEM image of a mouse brain during the peak of GH secretion.

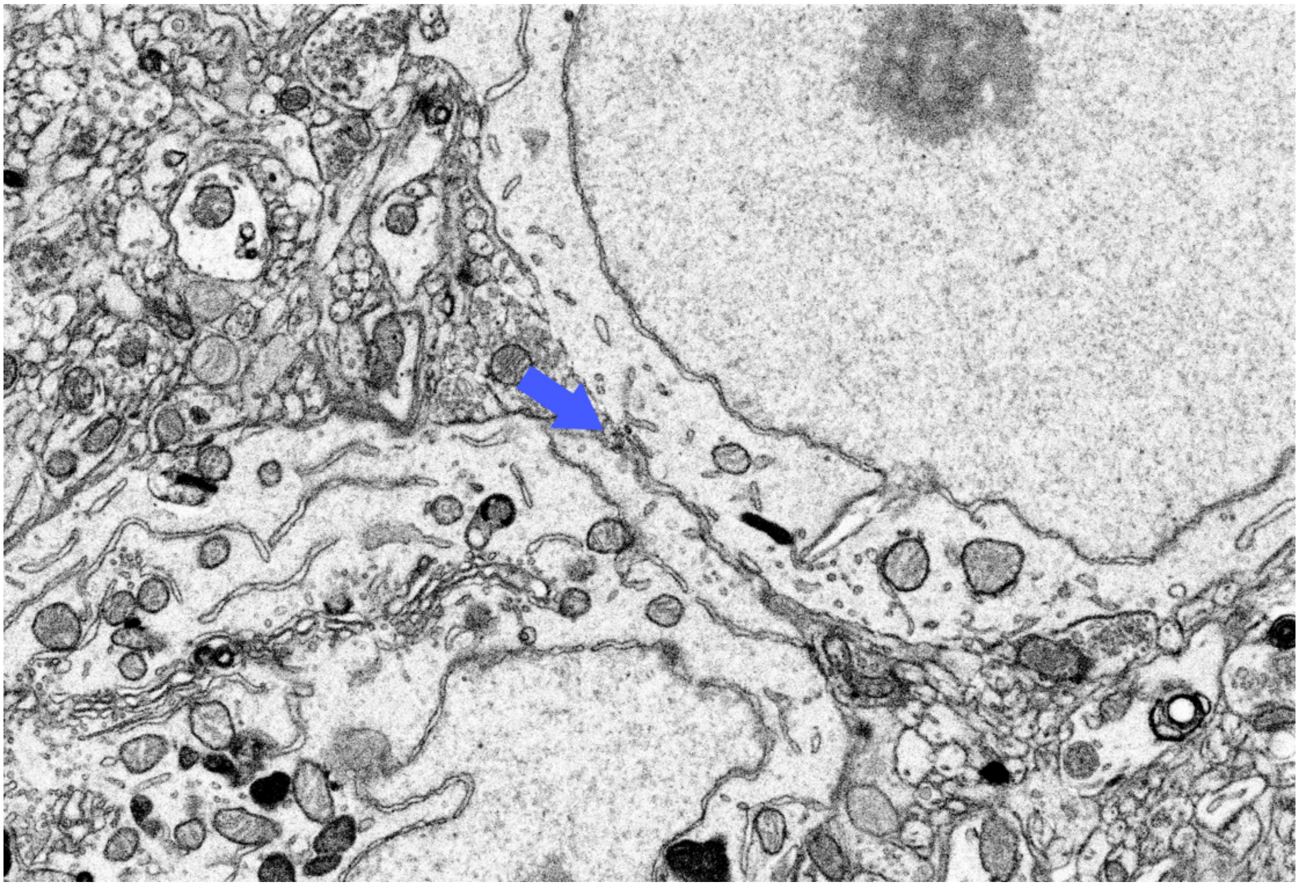

Fig.8. FIB-SEM image "slice" of a mouse brain during the peak of GH secretion. Blue arrow points to two neuronal membranes that are directly juxtaposed and not separated by astrocytic processes. In this way, more synapses can form.

Table 1. Summary of the dSTORM staining protocol.

	Inhibitory synapse		Excitatory synapse		GHRH cells
	Pre-synaptic	Post-synaptic	Pre-synaptic	Post-synaptic	
1’ Ab	VGAT (1:1000)	Gephyrin (1:500)	VGLUT2 (1:5000)	PSD 95 (1:2000)	GHRH (1:500)
2’ Ab	CF 568 (1:500)	Al 647 (1:500)	CF 568 (1:500)	Al 647 (1:500)	Al 488 (1:500)
Fixation	4% PFA – 15min		4% PFA – 15min		4% PFA – 15min
Blinking buffer	Cysteamine (MEA), 2-mercaptoethanol, Glucose oxidase (Gloxy)				-
Clearing buffer	Scale U2 buffer for 2 to max. 7 days				

References

(1) Retrieved June 23, 2019, from http://www.vivo.colostate.edu/hbooks/pathphys/endocrine/hypopit/gh.html

(2) Nyberg, F., & Hallberg, M. (2013). Growth hormone and cognitive function. Nature Reviews Endocrinology, 9(6), 357-365. doi:10.1038/nrendo.2013.78

(3) Grayzel, E. F. (1977). Growth hormone levels in acromegaly after external radiotherapy. Archives of Internal Medicine, 137(6), 808-809. doi:10.1001/archinte.137.6.808

(4) Feifel, D., Vaccarino, F. J. (1994). Growth hormone-regulatory peptides (GHRH and somatostatin) and feeding: A model for the integration of central and peripheral function. Neuroscience & Biobehavioral Reviews, 18(3), 421-433. doi:10.1016/0149-7634(94)90055-8

(5) Balthasar, N., Mery, P., Magoulas, C. B., Mathers, K. E., Martin, A., Mollard, P., Robinson, I. C. (2003). Growth Hormone-Releasing Hormone (GHRH) Neurons in GHRH-Enhanced Green Fluorescent Protein Transgenic Mice: A Ventral Hypothalamic Network. Endocrinology, 144(6), 2728-2740. doi:10.1210/en.2003-0006

(6) Tannenbaum, G. S. (1987). Physiological Significance of Somatostatin in Growth Hormone Regulation. Somatostatin, 169-182. doi:10.1007/978-1-4684-5326-3_16

(7) Tannenbaum, G. S., Martin, J. B. (1976). Evidence for an Endogenous Ultradian Rhythm Governing Growth Hormone Secretion in the Rat. Endocrinology, 98(3), 562-570. doi:10.1210/endo-98-3-562

(8) Hodges, J. (1970). The Hypothalamus and Pituitary ACTH Release. Progress in Brain Research Pituitary, Adrenal and the Brain, 12-20. doi:10.1016/s0079-6123(08)61514-9

(9) Jaffe, C. A., Ocampo-Lim, B., Guo, W., Krueger, K., Sugahara, I., Demott-Friberg, R., . . . Barkan, A. L. (1998). Regulatory mechanisms of growth hormone secretion are sexually dimorphic. Journal of Clinical Investigation, 102(1), 153-164. doi:10.1172/jci2908

(10) Baccam, N., Alonso, G., Costecalde, T., Fontanaud, P., Molino, F., Robinson, I. C., . . . Mery, P. (2007). Dual-Level Afferent Control of Growth Hormone-Releasing Hormone (GHRH) Neurons in GHRH-Green Fluorescent Protein Transgenic Mice. Journal of Neuroscience, 27(7), 1631-1641. doi:10.1523/jneurosci.2693-06.2007

(11) Osterstock, G., Escobar, P., Mitutsova, V., Gouty-Colomer, L., Fontanaud, P., Molino, F., . . . Méry, P. (2010). Ghrelin Stimulation of Growth Hormone-Releasing Hormone Neurons Is Direct in the Arcuate Nucleus. PLoS ONE, 5(2). doi:10.1371/journal.pone.0009159

(12) Zhang, Beaudet, & Tannenbaum. (2001). Sexually Dimorphic Expression of sst1 and sst2 Somatostatin Receptor Subtypes in the Arcuate Nucleus and Anterior Pituitary of Adults Rats. Journal of Neuroendocrinology, 11(2), 129-136. doi:10.1046/j.1365-2826.1999.00295.x

(13) Osterstock, G., Mitutsova, V., Barre, A., Granier, M., Fontanaud, P., Chazalon, M., . . . Méry, P. (2016). Somatostatin triggers rhythmic electrical firing in hypothalamic GHRH neurons. Scientific Reports, 6(1). doi:10.1038/srep24394

(14) Giustina, A., Wehrenberg, W. B. (1992). The role of glucocorticoids in the regulation of growth hormone secretion Mechanisms and clinical significance. Trends in Endocrinology & Metabolism,3(8), 306-311. doi:10.1016/1043-2760(92)90142-n

(15) Bridson, W. E., Kohler, P. O. (1970). Cortisol Stimulation of Growth Hormone Production by Human Pituitary Tissue in Culture. The Journal of Clinical Endocrinology & Metabolism, 30(4), 538-540. doi:10.1210/jcem-30-4-538

(16) Stroh, T., Schouwenburg, M. R., Beaudet, A., & Tannenbaum, G. S. (2009). Subcellular Dynamics of Somatostatin Receptor Subtype 1 in the Rat Arcuate Nucleus: Receptor Localization and Synaptic Connectivity Vary in Parallel with the Ultradian Rhythm of Growth Hormone Secretion. Journal of Neuroscience, 29(25), 8198-8205. doi:10.1523/jneurosci.0336-09.2009

(17) Theodosis, D. T. (2002). Oxytocin-Secreting Neurons: A Physiological Model of Morphological Neuronal and Glial Plasticity in the Adult Hypothalamus. Frontiers in Neuroendocrinology, 23(1), 101-135. doi:10.1006/frne.2001.0226

(18) Schultz, M. (2008). Rudolf Virchow. Emerging Infectious Diseases, 14(9), 1480-1481. doi:10.3201/eid1409.080667

(19) Types of glia. (2017, June 16). Retrieved from https://qbi.uq.edu.au/brain-basics/brain/brain-physiology/types-glia

(20) Whitteridge, D. (2013). Nerve Cells and Neuroglia. Res Medica, 3(2). doi:10.2218/resmedica.v3i2.384

(21) Eroglu, C., Barres, B. A. (2010). Regulation of synaptic connectivity by glia. Nature, 468(7321), 223-231. doi:10.1038/nature09612

(22) Santello, M., Calì, C., & Bezzi, P. (2012). Erratum to: Gliotransmission and the Tripartite Synapse. Synaptic Plasticity Advances in Experimental Medicine and Biology. doi:10.1007/978-3-7091-0932-8_26

(23) Christopherson, K. S., Ullian, E. M., Stokes, C. C., Mullowney, C. E., Hell, J. W., Agah, A., . . . Barres, B. A. (2005). Thrombospondins Are Astrocyte-Secreted Proteins that Promote CNS Synaptogenesis. Cell, 120(3), 421-433. doi:10.1016/j.cell.2004.12.020

(24) Iijima, T., Miura, E., Watanabe, M., & Yuzaki, M. (2010). Distinct expression of C1q-like family mRNAs in mouse brain and biochemical characterization of their encoded proteins. European Journal of Neuroscience. doi:10.1111/j.1460-9568.2010.07202.x

(25) Barker, A. J., Koch, S. M., Reed, J., Barres, B. A., & Ullian, E. M. (2008). Developmental Control of Synaptic Receptivity. Journal of Neuroscience, 28(33), 8150-8160. doi:10.1523/jneurosci.1744-08.2008

(26) Hama, H., Hara, C., Yamaguchi, K., & Miyawaki, A. (2004). PKC Signaling Mediates Global Enhancement of Excitatory Synaptogenesis in Neurons Triggered by Local Contact with Astrocytes. Neuron, 41(3), 405-415. doi:10.1016/s0896-6273(04)00007-8

(27) Iijima, T., Miura, E., Watanabe, M., & Yuzaki, M. (2010). Distinct expression of C1q-like family mRNAs in mouse brain and biochemical characterization of their encoded proteins. European Journal of Neuroscience. doi:10.1111/j.1460-9568.2010.07202.x

(28) Camandola, S. (2018). Astrocytes, emerging stars of energy homeostasis. Cell Stress, 2(10), 246-252. doi:10.15698/cst2018.10.157

(29) Dafny, N., & Feldman, S. (1970). Unit responses and convergence of sensory stimuli in the hypothalamus. Brain Research, 17(2), 243-257. doi:10.1016/0006-8993(70)90080-6

(30) Oomura, Y., Kimura, K., Ooyama, H., Maeno, T., Iki, M., & Kuniyoshi, M. (1964). Reciprocal Activities of the Ventromedial and Lateral Hypothalamic Areas of Cats. Science, 143(3605), 484-485. doi:10.1126/science.143.3605.484

(31) Chari M, Yang CS, Lam CK, Lee K, Mighiu P, Kokorovic A, Cheung GW, Lai TY, Wang PY, and Lam TK (2011). Glucose transporter-1 in the hypothalamic glial cells mediates glucose sensing to regulate glucose production in vivo. Diabetes 60(7): 1901–6. doi: 10.2337/db11-0120

(32) Verkhratsky A (2010). Physiology of neuronal-glial networking. Neurochem Int 7(4): 332–343. doi: 10.1016/j.neuint.2010.02.002

(33) Allard C, Carneiro L, Grall S, Cline BH, Fioramonti X, Chrétien C, Baba-Aissa F, Giaume C, Pénicaud L, and Leloup C (2014). Hypothalamic astroglial connexins are required for brain glucose sensing-induced insulin secretion. J Cereb Blood Flow Metab 34(2): 339–46. doi: 10.1038/jcbfm.2013.206

(34) Diano S, Kalra SP, and Horvath TL (1998). Leptin receptor immuno-reactivity is associated with the Golgi apparatus of hypothalamic neurons and glial cells. J Neuroendocrinol 10(9): 647–650.

(35) Dezonne RS, Lima FR, Trentin AG, and Gomes FC (2015). Thyroid hormone and astroglia: endocrine control of the neural environment. J Neuroendocrinol 27(6): 435–445. doi: 10.1111/jne.12283

(36) Cardona-Gómez GP, DonCarlos L, and Garcia-Segura LM (2000). Insulin-like growth factor I receptors and estrogen receptors colocalize in female rat brain. Neuroscience 99(4): 751–760. doi: 10.1016/s0306-4522(00)00228-1

(37) García-Cáceres C, Quarta C, Varela L, Gao Y, Gruber T, Legutko B, Jastroch M, Johansson P, Ninkovic J, Yi CX, Le Thuc O, Szigeti-Buck K, Cai W, Meyer CW, Pfluger PT, Fernandez AM, Luquet S, Woods SC, Torres-Alemán I, Kahn CR, Götz M, Horvath TL, and Tschöp MH (2016). Astrocytic Insulin Signaling Couples Brain Glucose Uptake with Nutrient Availability. Cell 166(4): 867–880. doi: 10.1016/j.cell.2016.07.028

(38) Reiner DJ, Mietlicki-Baase EG, McGrath LE, Zimmer DJ, Bence KK, Sousa GL, Konanur VR, Krawczyk J, Burk DH, Kanoski SE, Hermann GE, Rogers RC, and Hayes MR (2016). Astrocytes Regulate GLP-1 Receptor-Mediated Effects on Energy Balance. J Neurosci 36(12): 3531–3540. doi: 10.1523/JNEUROSCI.3579-15.2016

(39) García-Cáceres, C., Fuente-Martín, E., Burgos-Ramos, E., Granado, M., Frago, L. M., Barrios, V., . . . Chowen, J. A. (2011). Differential Acute and

Chronic Effects of Leptin on Hypothalamic Astrocyte Morphology and Synaptic Protein Levels. Endocrinology, 152(5), 1809-1818. doi:10.1210/en.2010-1252

(40) Horvath TL, Sarman B, García-Cáceres C, Enriori PJ, Sotonyi P, Shanabrough M, Borok E, Argente J, Chowen JA, Perez-Tilve D, Pfluger PT, Brönneke HS, Levin BE, Diano S, Cowley MA, and Tschöp MH (2010). Synaptic input organization of the melanocortin system predicts diet-induced hypothalamic reactive gliosis and obesity. Proc Natl Acad Sci U S A 107(33): 14875–14880. doi: 10.1073/pnas.1004282107

(41) He, J., Zhou, R., Wu, Z., Carrasco, M., Kurshan, P., Farley, J., . . . Zhuang, X. (2016). Prevalent Presence of Periodic Actin-spectrin-based Membrane Skeleton in a Broad Range of Neuronal Cell Types and Animal Species. doi:10.1101/045856

(42) Boettiger, A. N., Bintu, B., Moffitt, J. R., Wang, S., Beliveau, B. J., Fudenberg, G., . . . Zhuang, X. (2016). Super-resolution imaging reveals distinct chromatin folding for different epigenetic states. Nature, 529(7586), 418-422. doi:10.1038/nature16496

(43) Sahl, S. J., Lau, L., Vonk, W. I., Weiss, L. E., Frydman, J., & Moerner, W. E. (2015). Delayed emergence of subdiffraction-sized mutant huntingtin fibrils following inclusion body formation. Quarterly Reviews of Biophysics, 49. doi:10.1017/s0033583515000219

(44) Microscopy's Growth Through the Years. (n.d.). Retrieved from https://www.the-scientist.com/features/microscopys-growth-through-the-years-32775

(45) Galbraith, C. G., & Galbraith, J. A. (2011). Super-resolution microscopy at a glance. Journal of Cell Science, 124(10), 1607-1611. doi:10.1242/jcs.080085

(46) Hell, S. W., & Wichmann, J. (1994). Breaking the diffraction resolution limit by stimulated emission: Stimulated-emission-depletion fluorescence microscopy. Optics Letters, 19(11), 780. doi:10.1364/ol.19.000780

(47) Hell, S. W. (2002). Increasing the Resolution of Far-Field Fluorescence Light Microscopy by Point-Spread-Function Engineering. Topics in Fluorescence Spectroscopy, 361-426. doi:10.1007/0-306-47070-5_9

(48) Westphal, V., & Hell, S. W. (2005). Nanoscale Resolution in the Focal Plane of an Optical Microscope. Physical Review Letters, 94(14). doi:10.1103/physrevlett.94.143903

(49) Betzig, E., Patterson, G. H., Sougrat, R., Lindwasser, O. W., Olenych, S., Bonifacino, J. S., . . . Hess, H. F. (2006). Imaging Intracellular Fluorescent Proteins at Nanometer Resolution. Science,313(5793), 1642-1645. doi:10.1126/science.1127344

(50) Rust, M. J., Bates, M. and Zhuang, X. (2006). Subdiffraction-limit imaging by stochastic optical reconstruction microscopy (STORM). *Nat. Methods* 3, 793-795

(51) Bates, M., Blosser, T. R., & Zhuang, X. (2005). Short-Range Spectroscopic Ruler Based on a Single-Molecule Optical Switch. Physical Review Letters, 94(10). doi:10.1103/physrevlett.94.108101

(52) Linde, S. V., Löschberger, A., Klein, T., Heidbreder, M., Wolter, S., Heilemann, M., & Sauer, M. (2011). Direct stochastic optical reconstruction

microscopy with standard fluorescent probes. Nature Protocols, 6(7), 991-1009. doi:10.1038/nprot.2011.336

(53) Dempsey, G. T., Vaughan, J. C., Chen, K. H., & Zhuang, X. (2012). Evaluation of Fluorophores for Optimal Performance in Localization-Based Super-Resolution Imaging. Biophysical Journal,102(3). doi:10.1016/j.bpj.2011.11.3934

(54) Single-Molecule Super-Resolution Imaging. (n.d.). Retrieved from https://www.microscopyu.com/techniques/super-resolution/single-molecule-super-resolution-imaging

(55) Savtchenko, L. P., & Rusakov, D. A. (2007, February 06). The optimal height of the synaptic cleft. Retrieved from https://www.ncbi.nlm.nih.gov/pmc/articles/PMC1783902/

(56) Wegel, E., Göhler, A., Lagerholm, B. C., Wainman, A., Uphoff, S., Kaufmann, R., & Dobbie, I. M. (2016). Imaging cellular structures in super-resolution with SIM, STED and Localisation Microscopy: A practical comparison. Scientific Reports, 6(1). doi:10.1038/srep27290

(57) An Introduction to Electron Microscopy for Biologists. (2016, July 09). Retrieved from https://bitesizebio.com/29197/introduction-electron-microscopy-biologists/

(58) Scanning Electron Microscopy. (n.d.). Retrieved from https://www.nanoscience.com/techniques/scanning-electron-microscopy/

(59) Davuluri, P. (2018, April 06). An Introduction to Electron Microscopy - FIB. Retrieved from https://www.fei.com/introduction-to-electron-microscopy/fib/

(60) Sezen, M. (2016). Focused Ion Beams (FIB) — Novel Methodologies and Recent Applications for Multidisciplinary Sciences. Modern Electron Microscopy in Physical and Life Sciences. doi:10.5772/61634

(61) Steyn, F. J., Huang, L., Ngo, S. T., Leong, J. W., Tan, H. Y., Xie, T. Y., . . . Chen, C. (2011). Development of a Method for the Determination of Pulsatile Growth Hormone Secretion in Mice. Endocrinology, 152(8), 3165-3171. doi:10.1210/en.2011-0253

(62) Franklin, K. B., & Paxinos, G. (2012). The mouse brain in stereotaxic coordinates. Amsterdam: Elsevier.

(63) Paxinos, G. E. (1985). The Rat Nervous System; Volume 1: Forebrain and Midbrain. Orlando, FL, Academic Press.

(64) Richardson, D. S., & Lichtman, J. W. (2015). Clarifying Tissue Clearing. Cell, 162(2), 246-257. doi:10.1016/j.cell.2015.06.067

(65) Louhichi, S., Gzara, M., & Abdallah, H. B. (2014). A density based algorithm for discovering clusters with varied density. 2014 World Congress on Computer Applications and Information Systems (WCCAIS). doi:10.1109/wccais.2014.6916622

(66) Nahidiazar, L., Agronskaia, A. V., Broertjes, J., Broek, B. V., & Jalink, K. (2016). Optimizing Imaging Conditions for Demanding Multi-Color Super Resolution Localization Microscopy. Plos One, 11(7). doi:10.1371/journal.pone.0158884

(67) Dani, A., Huang, B., Bergan, J., Dulac, C., & Zhuang, X. (2010). Superresolution Imaging of Chemical Synapses in the Brain. Neuron, 68(5), 843-856. doi:10.1016/j.neuron.2010.11.021

(68) Pechstein, A., & Shupliakov, O. (2010). Taking a Back Seat: Synaptic Vesicle Clustering in Presynaptic Terminals. Frontiers in Synaptic Neuroscience, 2. doi:10.3389/fnsyn.2010.00143